

# Mechanics Informatics: A paradigm for efficiently learning constitutive models

Royal C. Ihuaenyi<sup>a</sup>, Wei Li<sup>a</sup>, Martin Z. Bazant<sup>b,c</sup>, Juner Zhu<sup>a,\*</sup>

<sup>a</sup>*Department of Mechanical and Industrial Engineering, Northeastern University, 360 Huntington Ave, Boston, 02115, MA, USA*

<sup>b</sup>*Department of Chemical Engineering, Massachusetts Institute of Technology, 77 Massachusetts Ave, Cambridge, 02139, MA, USA*

<sup>c</sup>*Department of Mathematics, Massachusetts Institute of Technology, 77 Massachusetts Ave, Cambridge, 02139, MA, USA*

---

## Abstract

Efficient and accurate learning of constitutive laws is crucial for accurately predicting the mechanical behavior of materials under complex loading conditions. Accurate model calibration hinges on a delicate interplay between the information embedded in experimental data and the parameters that define our constitutive models. The information encoded in the parameters of the constitutive model must be complemented by the information in the data used for calibration. This interplay raises fundamental questions: How can we quantify the information content of test data? How much information does a single test convey? Also, how much information is required to accurately learn a constitutive model? To address these questions, we introduce *mechanics informatics*, a paradigm for efficient and accurate constitutive model learning. At its core is the *stress state entropy*, a metric quantifying the information content of experimental data. Using this framework, we analyzed specimen geometries with varying information content for learning an anisotropic inelastic law. Specimens with limited information enabled accurate identification of a few parameters sensitive to the information in the data. Furthermore, we optimized specimen design by incorporating stress state entropy into a Bayesian optimization scheme. This led to the design of cruciform specimens with maximized entropy for accurate parameter identification. Conversely, minimizing entropy in Peirs shear specimens yielded a uniform pure shear stress state, showcasing the framework's flexibility in tailoring designs for specific experimental goals. Finally, we addressed experimental uncertainties and demonstrated the potential of transfer learning for replacing challenging

---

\*Corresponding author.

*Email address:* j.zhu@northeastern.edu (Juner Zhu)

testing protocols with simpler alternatives, while preserving calibration accuracy.

*Keywords:* Informatics, Inverse learning, Information theory, Entropy, Machine learning, Uncertainty quantification

---

## 1. Introduction

How many material parameters can be learned from a given experimental dataset? This question has been central to the field of mechanics for generations, with some of the greatest minds working to address it. In 1638, Galileo Galilei derived a single parameter from a simple experiment involving the deflection of a bar caused by a hanging weight (Galilei, 1638). The parameter he identified—the ratio of gravitational force to deflection—was later formalized by mechanics as the engineering stiffness of the bar, marking the beginning of elasticity theory. Between 1865 and 1925, Maxwell, Huber (1904), von Mises (1913), and Hencky (1924) observed the difference in materials strength in two types of tests (i.e., tensile and shear) and developed a yield theory based on the  $J_2$  invariant. In some sense, the two coefficients in the expression of the  $J_2$  invariant were successfully learned from two types of tests. In 1948, Rodney Hill expanded this  $J_2$  yield theory, learning six parameters from tensile and shear tests conducted in three orthogonal directions. His model (Hill, 1948), known as Hill’s 1948 criterion (Hill48), remains one of the most widely used models for describing anisotropy in yield surfaces. In a deterministic context,  $n$  material parameters can be derived from  $n$  distinct experiments. Consequently, advancements in experimental techniques have significantly enhanced the ability of modern mechanics to develop more sophisticated constitutive models.

With the abundance of constitutive models and the adequacy of theories, identifying their unknown parameters has become a critical task for researchers and engineers nowadays. These models describe intricate mechanical behaviors influenced by material microstructures, such as those seen in sheet metals during forming processes (Cao and Banu, 2020; Cao et al., 2024). While some physics-based parameters could be determined through first-principles quantum calculations (Qi et al., 2014; Dreyer et al., 2015; Chang et al., 2017), model parameters are more often identified through carefully executed mechanical tests (Rossi et al., 2022; Guery et al., 2016; Zhu et al., 2014). This paradigm of identifying model parameters is human-centered and not easily automated or optimized. Designing and conducting tests with simple stress states—such as uniaxial

tension, equi-biaxial tension, and simple shear—is essential. In an ideal situation, each simple test generates a desired stress state with only one non-trivial component, allowing the identification of one parameter at a time.

This traditional paradigm has proven successful in materials characterization and mechanical modeling across disciplines such as metal forming (Rossi et al., 2022) and automotive design (Fu et al., 2016, 2020; Anghileri et al., 2005), thanks to its robustness and interpretability. However, three significant limitations have emerged as experimental mechanics has evolved:

First, “simple” tests are not necessarily simple to perform. They are inevitably influenced by structural changes, such as rotation and necking. The ideal uniaxial or biaxial stress state is usually not achievable in practice. Uniaxial tension (UT) specimens are prone to strain localization, so the post-localization constitutive relation has to be obtained inversely (Dunand and Mohr, 2010; Kamaya and Kawakubo, 2011; Zhang et al., 1999). The stress state of uniaxial compression (UC) specimens is sensitive to the friction between the sample surface and the loading plate, thus turned into an “upsetting” test (Bao and Wierzbicki, 2004; Wierzbicki et al., 2005; Vilotic et al., 2003). Simple shear (SS) is often used as an alternative of pure shear because the former has lower requirement for force controlling in the direction perpendicular to the shear load (Segal, 2002). The design of SS specimen deals with eliminating the effect of rigid-body rotation and the bending moment on the critical section. Equi-biaxial (EB) tension tests request sophisticated designing of a cruciform specimen as well as the precise controlling of the loading device (Kuwabara et al., 1998; Kuwabara, 2007; Meng et al., 2016). The challenge is how to induce a large and uniform deformation in the region of interest. Usually, the central area has a reduced thickness, and grooves are introduced in the arms of the cruciform specimen. Given these experimental challenges, obtaining the intrinsic mechanical properties often requires sophisticated analyses, commonly aided by computational methods.

The second limitation is that simple tests provide limited information. This is because almost all the material points in the specimen of these tests are designed to undergo the same loading path, or at least in a small controlled range of stress state. The complete calibration of a complex constitutive model requires information about deformation in various states pertinent to the model parameters. As a result, multiple simple tests are needed, leading to a high experimental cost. In many real-world problems, experimental

resources are often limited or the operating cost is significantly higher than the material cost. For example, in order to observe the deformation mechanisms of microstructures, specimens are often placed under the monitoring of a scanning electron microscope (SEM), transmission electron microscope (TEM), or X-ray-based computer tomography (XCT) for in situ tests (Gorji and Mohr, 2017; Ni et al., 2021; Zhu et al., 2018). In such a situation, the total number of tests has to be small in order to control the overall cost. To achieve this goal, the amount of information that could be obtained from each single test must be increased.

Lastly, the human-centered paradigm requires extensive training for practitioners, who rely heavily on prior knowledge to design test specimens and perform post-test analyses. For instance, achieving an ideal in-plane shear state before shear fracture has led to the development of various simple shear specimens, designed through knowledge-intensive FEM simulations and optimizations (Dunand and Mohr, 2010, 2011; Morin et al., 2017; Gorji and Mohr, 2017; Tancogne-Dejean et al., 2021). This expertise is essential for automating specimen design and parameter identification in industrial applications. Furthermore, the technological advancements of the Industry 4.0 era present new challenges for engineering education—demanding a workforce skilled in automated manufacturing, digital-twin simulations, big data, and analytics (Hernandez-de Menendez et al., 2020). Thus, the current knowledge-intensive, human-centered paradigm must be re-envisioned to prepare engineering students for future careers.

Overcoming these limitations requires a *paradigm shift*: Test specimens with intricate geometries to maximize information in a single test and leveraging computer algorithms to extract useful data for parameter identification. Ortiz and co-workers established a comprehensive framework for data-driven computational solid mechanics in a series of publications (Kirchdoerfer and Ortiz, 2016, 2017, 2018; Stainier et al., 2019; Eggersmann et al., 2019; Carrara et al., 2020; Eggersmann et al., 2021). It was shown that this data-driven framework can be used to learn material laws. In order to increase the amount of information in a single test, the team employed a simple but effective design of specimens with multiple holes subject to bi-axial loading (Stainier et al., 2019). The same philosophy was used by other researchers. Jones et al. (2018) developed an iterative process to design a “D-shaped” test specimen. The test specimen was designed to enrich the deformation and stress fields generated in a uniaxial test for inverse parameter calibration

of a viscoplastic material model. A “ $\Sigma$ -shaped” test specimen, designed by Kim et al. (2014), was used in uniaxial tests to provide adequate mechanical heterogeneous information for the inverse identification of Hill48 model parameters. Additionally, Barroqueiro et al. (2020) presented a topologically optimized test specimen with a complex geometry. These designs were carefully analyzed and compared in our recent paper (Ihuaenyi et al., 2024).

As the complexity of test specimens and boundary conditions increases, it becomes impractical to analytically solve the stress and strain fields to determine the constitutive relationship directly. Consequently, learning the constitutive models of materials becomes an inverse problem. In deformable solids, the inverse problem is inherently overdetermined, meaning there are more equations than unknowns. Typically, it is addressed by optimizing a set of constitutive parameters for a chosen model, minimizing the difference between model predictions and experimental data. The success of this inverse learning process hinges on two key factors: a sufficiently large dataset and an effective optimization algorithm. Over the past three decades, advancements in these two areas have driven two significant ‘waves’ of inverse learning in mechanics.

The first wave was during the late 1990s and early 2000s. The maturation of the digital image correlation (DIC) technique (Sutton et al., 2009) made it possible to efficiently measure the full-field deformation pattern and history of a complex-geometry specimen at a low cost. Hence, a tremendously bigger database could be used for learning the constitutive relations inversely. Five different types of inverse methods were overviewed by Avril et al. (2008a). Among them, the finite element model updating (FEMU) method and the virtual fields method (VFM) have perhaps the widest applications. FEMU performs iteratively finite element (FE) simulations of the test to find the optimum set of constitutive parameters that can achieve the minimum deviation between model predictions and experimental observations (e.g. Dunand and Mohr, 2010; Zhang et al., 1999; Zhu et al., 2014). It has a low requirement for data. In particular, a complete set of full-field data of the entire domain is not a necessity. VFM is based on the principle of virtual work applied with well-chosen virtual fields (Avril et al., 2008b; Kramer and Scherzinger, 2014; Lattanzi et al., 2020). Because the calculation of the potential energy is an integral over the total volume, this method must be based on a full-field measurement. In most realistic situations, only the surface of the specimen could be monitored,

using VFM requires that the displacement field of the entire volume can be represented by or calculated from the surface information. A major challenge of the VFM is how to effectively construct virtual fields. For a constitutive relation with  $m$  unknown parameters,  $m$  virtual fields are required to generate  $m$  independent equations (Avril et al., 2008a).

We are now amid the second wave of rapid developments of inverse learning, which came with the great advancement of computational capability and the blooming of artificial intelligence (AI) algorithms, particularly deep learning. Successful applications of modern AI techniques in diverse scientific areas have enabled the recognition and prediction of phase patterns (Zhao et al., 2020, 2021, 2023), identification of material parameters (Yamanaka et al., 2020), visualization of safety envelopes (Li et al., 2019), and optimization of engineered systems (Attia et al., 2020; Aykol et al., 2021), to name a few examples. The progress in these computational areas sheds light on solving the inverse problem with higher efficiency to learn the mechanical constitutive relations. For example, Darve and co-authors (Huang et al., 2020; Xu et al., 2021) applied deep neural networks to determine constitutive parameters from “indirect observations” where the stress-strain pairs could not be explicitly obtained. Another example is automated and unsupervised learning codes developed by Kumar and De Lorenzis’s teams (Marino et al., 2023; Flaschel et al., 2021, 2023). In another example, (Deng et al., 2022) learned elastic chemo-mechanical constitutive relations and detected plastic deformation from atomic-scale imaging of 3D strain and concentration fields. Moreover, great progress has been achieved in developing data-driven representations of mechanical constitutive models, which can accelerate the inverse learning process. A comprehensive review could be found in a recent paper by Fuhg et al. (2024).

Despite these successful progresses, some fundamental questions remain unaddressed, posing challenges to the *paradigm shift* from the traditional human-centered multi-test identification to the AI-assisted single-test inverse learning.

**Question #1.** How much information does a single test convey?

**Question #2.** How much information is required to accurately learn a model?

**Question #3.** How can we optimally design test specimens to meet a target information content?

Inspired by *materials informatics* (Ramprasad et al., 2017) and *medical informat-*

ics (Haux, 2010), we introduce the concept of *mechanics informatics* to answer these questions. The central idea is to leverage principles from information theory and data science to enhance the design of experiments, refine the selection and calibration of constitutive models, and ensure the reliability of modeling outcomes. In this paper, we will systematically elaborate on the definition and application of this important informatics concept.

## 2. Problem formulation of learning constitutive models

### 2.1. Governing equations

For a deformable domain  $\Omega \subset \mathbb{R}^d$ , the strain-displacement kinematic relationship is defined by

$$\boldsymbol{\varepsilon}(\mathbf{u}) = \frac{1}{2}(\nabla \mathbf{u} + \nabla \mathbf{u}^\top), \quad \text{in } \Omega, \quad (1)$$

where  $\boldsymbol{\varepsilon}$  denotes the strain tensor and  $\mathbf{u}$  is the displacement field. The Dirichlet boundary condition prescribed on  $\Omega_u$  is given by

$$\mathbf{u} = \hat{\mathbf{u}}, \quad \text{on } \Omega_u, \quad (2)$$

where  $\hat{\mathbf{u}}$  represents the prescribed displacement field along the boundary.

The equilibrium condition for forces within the domain is expressed as

$$\text{div } \boldsymbol{\sigma} + \mathbf{b} = \mathbf{0}, \quad \text{in } \Omega, \quad (3)$$

where  $\boldsymbol{\sigma}$  is the stress tensor and  $\mathbf{b}$  is the body force vector. Additionally, the Neumann boundary condition applied on  $\Omega_t$  is given by

$$\boldsymbol{\sigma} \mathbf{n} = \hat{\mathbf{t}}, \quad \text{on } \Omega_t, \quad (4)$$

where  $\mathbf{n}$  is the unit normal to the boundary and  $\hat{\mathbf{t}}$  represents the prescribed traction. Together, these equations govern the behavior of the deformable domain  $\Omega$  under applied displacements and forces.

### 2.2. Constitutive relations

A general form of the constitutive relation is expressed as

$$\boldsymbol{\sigma} = \boldsymbol{\sigma}(\boldsymbol{\varepsilon}, \dot{\boldsymbol{\varepsilon}}, T), \quad (5)$$

where  $\dot{\boldsymbol{\varepsilon}}$  represents the strain rate, and  $T$  denotes the temperature. In this study, we focus on material models that are independent of strain rate and temperature, simplifying the constitutive relation to  $\boldsymbol{\sigma} = \boldsymbol{\sigma}(\boldsymbol{\varepsilon})$ . This approach follows small-deformation plasticity theory, a widely used framework for modeling sheet metals, based on the additive decomposition of the strain tensor:

$$\boldsymbol{\varepsilon} = \boldsymbol{\varepsilon}^e + \boldsymbol{\varepsilon}^p, \quad (6)$$

where  $\boldsymbol{\varepsilon}^e$  and  $\boldsymbol{\varepsilon}^p$  are the elastic and plastic components of the strain tensor, respectively.

The Cauchy stress is determined by the elastic response as

$$\boldsymbol{\sigma} = \mathbb{C} : \boldsymbol{\varepsilon}^e, \quad (7)$$

where  $\mathbb{C}$  is the fourth-order elastic modulus tensor.

The yielding behavior of the material is governed by a yield function, defined as

$$f(\boldsymbol{\sigma}, \boldsymbol{\varepsilon}^p) = 0. \quad (8)$$

Furthermore, the plastic flow is characterized by the relation

$$\dot{\boldsymbol{\varepsilon}}^p = |\dot{\boldsymbol{\varepsilon}}^p| \frac{\partial g(\boldsymbol{\sigma}, \boldsymbol{\varepsilon}^p)}{\partial \boldsymbol{\sigma}}, \quad (9)$$

where  $g$  is the flow potential function. When  $g$  is identical to the yield function  $f$ , the plastic flow is termed *associative*; otherwise, it is *non-associative* (Simo and Hughes, 2006; Gurtin et al., 2010).

Additionally, for characterizing how stress states evolve relative to the yield surface, the Kuhn-Tucker loading-unloading conditions are expressed as

$$|\dot{\boldsymbol{\varepsilon}}^p| \geq 0, \quad f \leq 0, \quad |\dot{\boldsymbol{\varepsilon}}^p| f = 0, \quad (10)$$

along with the consistency condition

$$|\dot{\boldsymbol{\varepsilon}}^p| \dot{f} = 0. \quad (11)$$

### 2.3. Forward and inverse problems

Equations 1 through 5 (with Eq. 5 detailed by Eqs. 6 to 11) fully describe a boundary value problem (BVP) that can be solved for a unique solution when appropriate boundary



conditions are specified, and the parameters of the constitutive relations are known. This formulation defines the forward problem as follows:

$$\text{Forward problem: } \{\hat{\mathbf{u}}, \hat{\mathbf{t}}, \boldsymbol{\theta}\} \longrightarrow \{\mathbf{u}(\mathbf{x}), \boldsymbol{\varepsilon}(\mathbf{x}), \boldsymbol{\sigma}(\mathbf{x})\}, \quad (12)$$

where  $\boldsymbol{\theta}$  represents the parameter vector or parameter space associated with the constitutive framework.

Solving the forward problem is essential when material properties are fully characterized, and the parameter space is known, as it facilitates the prediction of stress fields. The forward problem is well-posed, ensuring both the uniqueness and existence of a solution given the defined parameters. However, in many practical scenarios, the parameter space  $\boldsymbol{\theta}$  that defines the constitutive model is totally or partially unknown. This uncertainty often arises from the complex nature of material responses, which necessitates constitutive models involving parameters that are challenging to identify experimentally with high reliability. In such cases, the problem must be approached inversely:

$$\text{Type-I Inverse problem: } \{\mathbf{u}(\mathbf{x}) \rightarrow \boldsymbol{\varepsilon}(\mathbf{x}), \hat{\mathbf{t}}\} \longrightarrow \{\boldsymbol{\sigma}(\mathbf{x}), \boldsymbol{\theta}\}. \quad (13)$$

In most continuum models, the parameter space  $\boldsymbol{\theta}$  comprises material parameters that are invariant with respect to the material coordinates  $\mathbf{x}$ . However, some advanced models incorporate material heterogeneity and anisotropy, making the parameter space coordinate-dependent (Ihuaenyi et al., 2021, 2023a,b; Iqbal et al., 2023). Theoretically, kinematic, equilibrium and constitutive equations hold at every material point, resulting in an over-determined system for the inverse problem. This over-determined nature of the problem often requires identifying the parameter space from noisy experimental observations, inherently rendering the inverse problem ill-posed due to potential issues with non-uniqueness or even non-existence of a solution. Additionally, the accuracy of parameter identification relies heavily on the robustness of the inverse learning procedure, which must not only capture the bulk material response effectively through informative test data but also demonstrate robustness to measurement noise.

It is noteworthy that efforts have been made to directly predict the stress field from full-field displacement measurements without explicitly defining a constitutive relation, such as in the study by Cameron and Tasan (2021).

$$\text{Type-II Inverse problem : } \{\mathbf{u}(\mathbf{x}) \rightarrow \boldsymbol{\varepsilon}(\mathbf{x}), \hat{\mathbf{t}}\} \xrightarrow{\text{Assumptions}} \{\boldsymbol{\sigma}(\mathbf{x})\}. \quad (14)$$

In such cases, the problem becomes under-determined, necessitating reasonable assumptions to reach a solution. For instance, Cameron and Tasan (2021) employed an “alignment assumption,” which posits that the principal directions of the Cauchy stress coincide with those of either the strain or strain rate. The viability of directly inferring stress from displacement thus hinges on the general applicability of these assumptions. In a sense, these assumptions operate as a simplified constitutive constraint that bypasses parameter specification. Consequently, the inverse problem expression in Eq. 14 can be regarded as a special case of Eq. 13. In this study, we concentrate on the Type-I inverse problems characterized by Eq. 13.

#### 2.4. A special case of anisotropic plasticity

In this study, we focus on a special case of the outlined constitutive framework, particularly examining the behavior of anisotropic sheet metal under a planar stress state. Initially, in the small deformation range, the material exhibits isotropic linear elasticity, described by its elastic modulus ( $E$ ) and Poisson’s ratio ( $\nu$ ).

As the material deforms plastically, its response transitions to that of an anisotropic model represented by a quadratic yield function. This yield function is coupled with an associated flow rule and an isotropic hardening law to capture the progression of the plastic deformation. The onset of plastic deformation is governed by the yield function, expressed as:

$$f(\boldsymbol{\sigma}, \boldsymbol{\varepsilon}^p) = \sqrt{\boldsymbol{\sigma} : \mathbf{A} : \boldsymbol{\sigma}} - \sigma_Y(\bar{\boldsymbol{\varepsilon}}^p) = 0, \quad (15)$$

where  $\mathbf{A}$  is a symmetric tensor characterizing material anisotropy. In the Hill48 (Hill, 1948) formulation, this tensor is defined as:

$$\mathbf{A} = \begin{bmatrix} 1 & -H & -G & 0 & 0 & 0 \\ -H & H + F & -F & 0 & 0 & 0 \\ -G & -F & F + G & 0 & 0 & 0 \\ 0 & 0 & 0 & 2L & 0 & 0 \\ 0 & 0 & 0 & 0 & 2M & 0 \\ 0 & 0 & 0 & 0 & 0 & 2N \end{bmatrix}. \quad (16)$$

Here,  $H$ ,  $G$ ,  $F$ ,  $L$ ,  $M$ , and  $N$  are yield constants, typically determined experimentally. Under the plane stress assumption, the stress components  $\sigma_{33} = \tau_{23} = \tau_{13} = 0$ , rendering the coefficients  $M$  and  $N$  irrelevant to the formulation. Notably, when the anisotropic

parameters take values  $F = G = H = 0.5$  and  $N = 1.5$ , the anisotropic yield surface simplifies to the isotropic von Mises yield surface.

Furthermore, the isotropic hardening law  $\sigma_Y(\bar{\varepsilon}^p)$  is modeled using the Swift formulation, expressed as:

$$\sigma_Y(\bar{\varepsilon}^p) = A(\bar{\varepsilon}^p + \varepsilon_0)^n. \quad (17)$$

In the inverse learning procedure, six parameters ( $A$ ,  $\varepsilon_0$ ,  $n$ ,  $F$ ,  $G$ , and  $N$ ) that characterize the material response are to be identified. This reduced parameter set is sufficient because the relationship  $H + G = 1$  is enforced by using the initial yield stress in the rolling direction (RD) as the reference yield stress.

### 3. Mechanics informatics

Mechanics informatics is introduced in this work as a framework aimed at addressing key challenges in quantifying the information content of mechanical tests and enabling the efficient and accurate learning of material laws. By evaluating the information content and richness of test data, this framework seeks to address the critical question: *"How much information does a single test convey?"*. Additionally, we consider the complementary question: *"How much information is required to accurately learn a constitutive model?"*. These questions are fundamental in mechanics since each test carries a unique amount and type of information. A material law represents the material's response under specific stress states, requiring a defined level of information from tests for learning. This framework offers a pathway to address these questions for efficient and accurate learning of material laws.

#### 3.1. Information entropy

Information theory, a groundbreaking framework pioneered by Shannon in 1948, provides the essential tools to quantify, encode, and transmit information across varied systems. At its core lies the concept of *entropy*, a fundamental measure of uncertainty or information content within a dataset, signal, or system. In essence, systems with greater complexity or variability reflect higher entropy, while those with more predictable patterns exhibit lower entropy, indicating redundancy.

To formally define information entropy, consider a discrete random variable  $X$  that takes on values  $\{x_1, x_2, \dots, x_n\}$ , where  $n$  represents the total number of possible outcomes.

The probability of observing a specific outcome  $x$  is given by  $p(x)$ . The entropy,  $H(X)$  of this variable, representing the average level of “surprise” or uncertainty across its outcomes, is calculated by the formula:

$$H(X) = - \sum_{x \in X} p(x) \ln p(x). \quad (18)$$

Since  $p(x) > 0$  and  $\sum_{x \in X} p(x) = 1$ , the minimum entropy  $H_{\min} = 0$  is achieved if a single outcome  $x_0$  occurs with probability  $p(x_0) = 1$ .

For continuous cases, where  $X$  is a random variable with a probability density function  $f(x)$ , the entropy generalizes to the form:

$$H(X) = - \int f(x) \ln f(x) dx, \quad (19)$$

which is minimized ( $H = 0$ ) when the continuous probability density is localized on one point outcome as a Dirac delta function,  $f(x) = \delta(x - x_0)$ .

By extension, if we consider two related discrete-valued variables  $X$  and  $Y$ , with  $p(y)$  representing the probability of any  $y \in Y$ , where  $Y$  is the set of all possible values  $\{y_1, y_2, \dots, y_n\}$ , the joint entropy associated with these variables is defined as:

$$H(X, Y) = - \sum_{x \in X} \sum_{y \in Y} p(x, y) \ln p(x, y). \quad (20)$$

Consequently, if the variables  $X$  and  $Y$  are continuous with a joint probability density function  $f(x, y)$ , their joint entropy is given by:

$$H(X, Y) = - \iint f(x, y) \ln f(x, y) dx dy. \quad (21)$$

When an independent relationship exists between the probability distributions of the two variables, their joint entropy can be expressed as the sum of their individual entropy values.

Additionally, the concept of maximum entropy is a fundamental aspect of information theory. A system reaches maximum entropy when the probabilities of all possible values of the discrete variable span a uniform distribution, which is expressed as:

$$H_{\max}(X) = - \ln \left( \frac{1}{n} \right). \quad (22)$$

### 3.2. Stress state analysis

The stress state of a material encapsulates the complex distribution of stresses arising from its composition, loading conditions, and boundary constraints. Different stress states can be induced in a test depending on the specific mechanical response or features targeted for extraction by a testing protocol. For instance, to characterize a material’s uniaxial tensile (UT) behavior, a standard dog-bone tensile specimen is typically employed. The gage section of this specimen is subjected to a pure uniaxial tensile stress as the tensile specimen is loaded primarily along one principal direction, with only one non-zero nominal stress:  $\boldsymbol{\sigma} = (\sigma_{11}, 0, 0, 0, 0, 0)^T$ .

Hence, to precisely capture material behavior under pure stress states, specialized testing methods have been developed, ensuring a robust and accurate representation of the bulk material properties. For uniaxial compression (UC) response, dog-bone-shaped specimens with a short gage length and stack compression tests are widely utilized (Alves et al., 2011; ASTM International, 2000). The torsion test is a standard approach applied for characterizing shear response using cylindrical or tubular specimens (Papasidero et al., 2015). Additionally, test specimens have been designed in literature to induce a pure shear stress state within a given gage section by normal stresses on the test specimen (Gorji and Mohr, 2017; Bao and Wierzbicki, 2004). Furthermore, testing methods such as the cruciform specimen test (Deng et al., 2015), hydraulic bulge test (Mulder et al., 2015), and mini-punch test (Roth and Mohr, 2016) have been effectively implemented in representing the equibiaxial tensile response of materials.

These testing configurations ensure that the resulting strain field or force response accurately reflects the material’s bulk response under each specific stress state. While these traditional tests are robust, they are designed to provide detailed information about the material behavior under a single stress state in each test. However, heterogeneous stress states can be induced through the design of test specimens with complex geometries, thereby enriching the information content of the data obtained from a single testing protocol (Kim et al., 2014; Barroqueiro et al., 2020; Jones et al., 2018). The variation in stress states within a single test reflects the diverse range of mechanical responses that can be captured. Hence, test protocols that can generate heterogeneous stress states within a single experiment, are valuable for reducing experimental costs when learning complex material models.

Analyzing the stress state within a given testing protocol is critical for selecting the appropriate experimental procedures for generating data to learn constitutive models. To accurately quantify the stress state(s) in a given test, it is essential to define metrics that characterize the nature of the applied loading conditions. Such metrics can include the ratios of principal stresses and their respective signs. For example, in the case of an isotropic material subjected to a planar stress state under pure uniaxial tension, only one principal stress is non-zero and positive ( $\sigma_{11} > 0$ ,  $\sigma_{22} = 0$ ). Conversely, in pure shear, the principal stress ratio equals  $-1$ , and the principal stresses exhibit opposite signs ( $\sigma_{11}/\sigma_{22} = -1$ ,  $\sigma_{11} > 0$ ,  $\sigma_{22} < 0$ ). In the context of anisotropic plasticity, as considered in this study, the stress state of a material undergoing plastic deformation can be described using two non-dimensionalized parameters: the stress triaxiality ( $\eta$ ) and the Lode angle parameter ( $\bar{\theta}$ ). The stress triaxiality  $\eta$ , serves as a measure of the relative contribution of hydrostatic stress within the overall stress state, defined as the ratio of hydrostatic stress to the equivalent stress:

$$\eta = \frac{\sigma_h}{\sigma_{\text{eqv}}}, \quad (23)$$

where  $\sigma_h = \frac{\sigma_{kk}}{3}$ , with  $\sigma_{kk}$  representing the first invariant or trace of the stress tensor, and  $\sigma_{\text{eqv}}$  is the equivalent stress. For a two-dimensional stress state, the stress triaxiality is constrained within the range  $\eta \in [-\frac{2}{3}, \frac{2}{3}]$ . In a general multiaxial stress state, the values of  $\eta$  can range from  $-\infty$  to  $\infty$ .

The Lode angle, which quantifies the deviatoric nature of the stress state, is expressed in terms of the normalized third invariant of the deviatoric stress tensor,  $J_3$ , as:

$$\cos(\theta) = \frac{27 J_3}{2 \sigma_{\text{eq}}^3}. \quad (24)$$

The Lode angle is often normalized within the range  $\bar{\theta} \in [-1, 1]$  as the Lode angle parameter:

$$\bar{\theta} = 1 - \frac{2}{\pi} \arccos\left(\frac{27 J_3}{2 \sigma_{\text{eq}}^3}\right). \quad (25)$$

Employing the stress triaxiality and Lode angle parameter as metrics, it is possible to precisely identify the stress state corresponding to a specific mechanical response during plastic deformation. This framework can be extended to evaluate the information content of stress states in a given testing protocol. Figure 1 illustrates the major stress states on a 2D yield surface of a material exhibiting tension-compression symmetry. The stress

triaxiality and Lode angle values are shown for each stress state, which characterizes the material's response under different loading conditions.

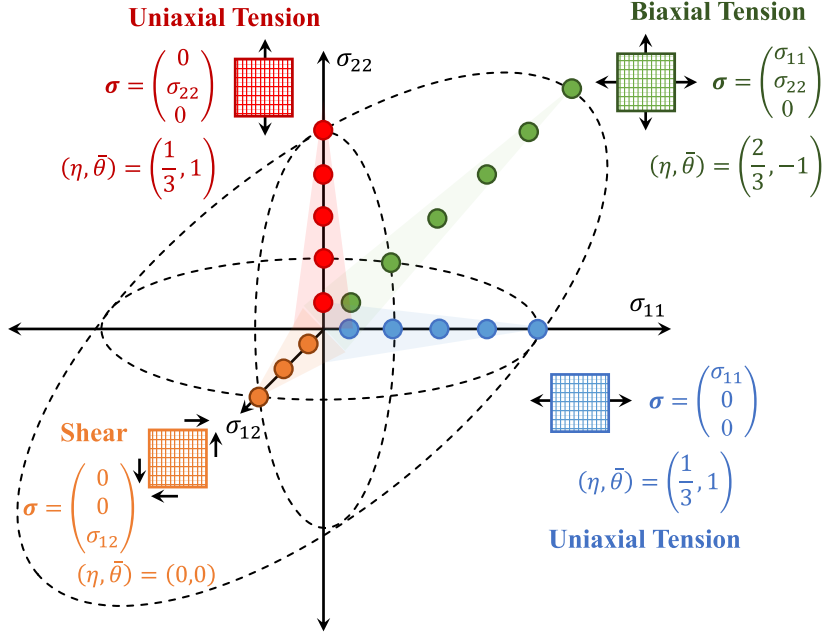


Figure 1: Two-dimensional yield surface exhibiting tension-compression symmetry, annotated with key stress states and their corresponding stress triaxiality and Lode angle parameter values.

### 3.3. Stress state entropy

In a previous work (Ihuaenyi et al., 2024), we proposed a theoretical framework that integrates concepts from information theory to quantify the information content of the stress state in test specimens subjected to specific loading conditions. Here, we summarize the mathematical framework for the *stress state entropy*, which serves as a measure of the information content in a mechanical test, incorporating stress metrics and information-theoretic principles.

Given  $\Theta$ , the set of all considered stress states required for feature extraction that can be generated from a test specimen  $S$ , and  $p(\sigma)$ , the probability of any stress state  $\sigma \in \Theta$ , the stress state information content or stress state entropy of the test specimen considering  $\Theta$  as a discrete-valued variable is defined as:

$$H(\Theta) = - \sum_{\sigma \in \Theta} p(\sigma) \ln p(\sigma). \quad (26)$$

To address the fundamental question, *How much information does a single test convey?*, the amount of information conveyed by a single test is its stress state entropy. By spatially discretizing the specimen geometry, we can analyze the local stress state in each

discrete region and by applying Equation 26, we can compute the stress state entropy for the entire specimen. This provides a clear metric for evaluating how informative a specimen’s response is under a given testing protocol.

To address the complementary question, *How much information is required to learn a constitutive model?*, we highlight the importance of analyzing both the model parameters and the stress states to which they are sensitive, as these factors influence their accurate identification. For example, a simple 1–D isotropic linear elastic model with a parameter space comprising of just the elastic modulus  $\theta = \{E\}$  can be accurately learned from a single uniaxial tensile test. This is because the material response under the uniaxial stress state provides sufficient information for parameter estimation. Thus, the informational requirement for this model corresponds to the stress state entropy for a stress state space associated with only uniaxial tension,  $\Theta = \{\sigma_{UT}\}$ . However, for more complex models, where parameters depend on responses across multiple stress states, accurate identification necessitates test data covering a broader range of the relevant stress states.

To effectively learn the anisotropic inelastic material model within the current formulation, which assumes a state of planar stress and tension-compression symmetry, the test database must encompass stress states that the material parameters are sensitive to. Specifically, the hardening law parameters  $(A, \varepsilon_0, n)$  and the yield constant  $G$  are primarily influenced by the uniaxial tensile response in the RD. The yield constants  $F$  and  $N$  are sensitive to the material response in the transverse direction (TD) and pure shear, respectively. Therefore, accurately identifying the material law requires test data capturing sufficient information from uniaxial tension in both the RD and TD, as well as pure shear ( $\Theta = \{\sigma_{UT}^{RD}, \sigma_{UT}^{TD}, \sigma_S\}$ ). Thus, the information required to accurately learn the material law is the *stress state entropy*, which considers all stress states required to learn the material law.

Furthermore, maximizing the stress state entropy of a test specimen requires a uniform probability distribution of stress states within the relevant stress state space. A specimen that achieves the maximum stress state entropy is defined as the *theoretically optimal specimen*. The stress state entropy of such a specimen is defined as:

$$H_{\max}(\Theta | = n) = -\ln\left(\frac{1}{n}\right). \quad (27)$$

Designing test specimens to achieve the maximally achievable stress state entropy within a given stress state space necessitates advanced topological optimization tech-



niques. However, the practical realization of such specimens can be constrained by uncertainties arising from impure stress states at specimen boundaries and experimental noise. To address these limitations, in (Ihuaenyi et al., 2024) we proposed an optimal stress state entropy hypothesis, which bounds the entropy of a test specimen designed to extract information about a specific stress state space between two limits, determined by the cardinality of the stress state space. This is defined as:

$$H_{\max}(\Theta | = n - 1) < H(\Theta | = n) \leq H_{\max}(\Theta | = n). \quad (28)$$

In essence, Equation 28 establishes that for a stress state space  $\Theta$  with cardinality  $n$ , the stress state entropy of the designed or selected specimen should exceed the maximum entropy associated with a stress state space of cardinality  $n - 1$  while remaining less than or equal to the maximum entropy for the complete stress state space. This bound ensures that all required stress states for learning the considered material law are represented in the test specimen response. This criterion provides a practical guideline for experimentalists to optimize the information extracted from test specimens, ultimately enhancing the accuracy of inverse learning for constitutive models that rely on material responses across multiple stress states.

#### 4. Inverse learning

In this work, we will inversely learn the parameters of the anisotropic inelastic material law from strain fields generated by test specimens of various geometries, subjected to different boundary conditions, with each specimen contributing data that offers distinct information content. Solving the inverse problem is realized through the penalization of the discrepancy between synthetic experimental strain fields and numerical strain fields. The synthetic experimental strain fields are generated from FE simulations using the ground truth parameter values as input and applying a typical DIC resolution limit to the strain fields. The measurement accuracy and strain resolution limit of DIC is highly dependent on system setup, speckle pattern quality, and environmental conditions (Sutton et al., 2009; Pan et al., 2009). In large deformation testing, such as for anisotropic materials, large strains tend to distort the speckle pattern, making it harder to track small displacements accurately. In this study, we apply a strain resolution limit of 0.05% to FE strain fields obtained from simulations of selected geometries. At strain levels below

this threshold, the mismatch between experimental and numerical strain fields becomes pronounced. This mismatch level between FE strain fields and experimental strain fields is typical in carefully carried out large deformation tests (Lava et al., 2020). The penalized mismatch is realized through an objective function defined as:

$$\mathcal{L}_{\boldsymbol{\theta}} = \frac{1}{n_p} \sum_{i=1}^{n_s} \sum_{j=1}^{n_p} \|\hat{\boldsymbol{\varepsilon}}_j - \boldsymbol{\varepsilon}_j(\boldsymbol{\theta})\|^2, \quad (29)$$

where  $\hat{\boldsymbol{\varepsilon}}_j = [\hat{\varepsilon}_{11}, \hat{\varepsilon}_{22}, \hat{\varepsilon}_{12}]_j$  is the experimental strain tensor,  $\boldsymbol{\varepsilon}_j(\boldsymbol{\theta}) = [\varepsilon_{11}(\boldsymbol{\theta}), \varepsilon_{22}(\boldsymbol{\theta}), \varepsilon_{12}(\boldsymbol{\theta})]_j$  is the numerical strain tensor with  $\boldsymbol{\theta}$  representing the parameter vector.  $n_p$  is the number of measurement points, and  $n_s$  is the number of time steps considered. In this work,  $n_s = 1$ .

#### 4.1. Parameter optimization

A deterministic optimization approach is employed to learn the model parameters by minimizing the objective function,  $\mathcal{L}_{\boldsymbol{\theta}}$ , using the Nelder–Mead simplex method (Lagarias et al., 1998; Singer and Nelder, 2009). The Nelder–Mead algorithm was chosen for its simplicity, versatility, and the distinct advantage of not requiring gradient information. This makes it especially well-suited for optimization problems where derivatives are either unavailable or computationally expensive. Additionally, the Nelder–Mead algorithm is effective for incorporating constraint functions, which is essential for ensuring that the parameters remain within physically meaningful bounds during optimization.

Although the Nelder-Mead algorithm is robust, it is widely recognized that its tendency to converge to local minima, particularly in high-dimensional and complex problem spaces, can limit its effectiveness. To address this challenge, we implemented a stringent convergence criterion to enhance the reliability of the optimization. Specifically, the optimization was terminated when the relative change in parameter values between successive iterations reached a threshold of  $1 \times 10^{-6}$ .

#### 4.2. Test specimen geometry and FE simulation

To investigate the influence of test specimen information content on accuracy in learning the material law, selected test specimen geometries are considered. The specimens are chosen based on the variations in their geometric complexity, presenting test cases for specimens with different stress state information content. The first two specimens are

designed for uniaxial testing conditions, where one end is fixed, and a uniform displacement is applied at the opposite end in the RD. These specimens, subjected to uniaxial tensile boundary conditions are the ubiquitous “*dog-bone*” uniaxial tension specimen and the  $\Sigma$ -shaped specimen intuitively designed by (Kim et al., 2014). We then consider a central region of the biaxial cruciform specimen, subjected to a biaxial tension loading state with the sample stretched in the RD and TD. Figure 2 illustrates the specimen geometries highlighting their corresponding regions of interest (ROI) and their dimensions in millimeters. The ROI for the dog-bone specimen consists of the area within its gage length experiencing a uniform uniaxial stress state. The entire area of the  $\Sigma$ -shaped specimen constitutes its ROI, while one-quarter of the cruciform specimen is considered as its ROI due to its geometric symmetry.

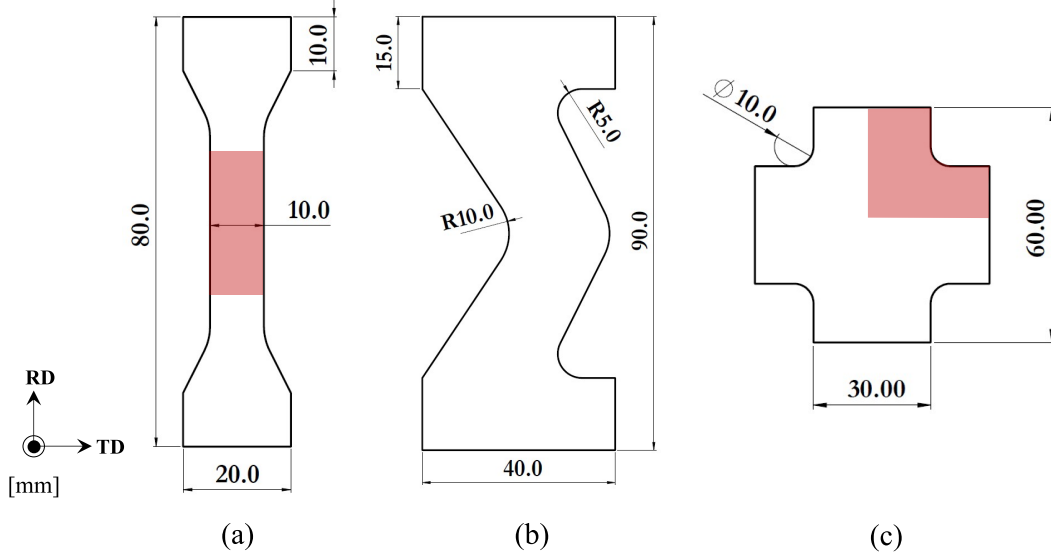


Figure 2: Test specimen geometries considered for inverse learning: (a) Uniaxial tension specimen, (b)  $\Sigma$ -shaped specimen (Kim et al., 2014), and (c) cruciform specimen.

FE simulations were carried out using the ABAQUS/EXPLICIT<sup>®</sup> solver, employing 8-noded brick elements with reduced integration and hourglass control to ensure numerical stability. A fine mesh was adopted that strikes a balance between computational efficiency and the smoothness of the resulting strain fields. All simulations were designed to meet the specific boundary condition requirements of the specimens under study. For the uniaxial tension and  $\Sigma$ -shaped specimens, one end was fixed while a displacement of 2 mm was applied along the RD. For the cruciform specimen, a displacement of 2 mm was applied simultaneously along both the RD and the TD. The magnitude of the displacement was kept consistent between all specimens to maintain comparability.

### 4.3. Specimen information content

Here, we analyze the stress state information content of the considered specimen geometries through the stress state entropy computed using Equation 26. In this analysis, the information content of the specimens is examined under the assumption of no prior knowledge of the ground truth anisotropic inelastic response. Accordingly, the stress fields are generated using the known von Mises parameters. To also qualitatively assess the stress state richness of each test specimen, Figure 3 presents a visual representation of the stress distribution of the specimen geometries, plotted on the  $\sigma_{11}$  and  $\sigma_{22}$  yield loci.

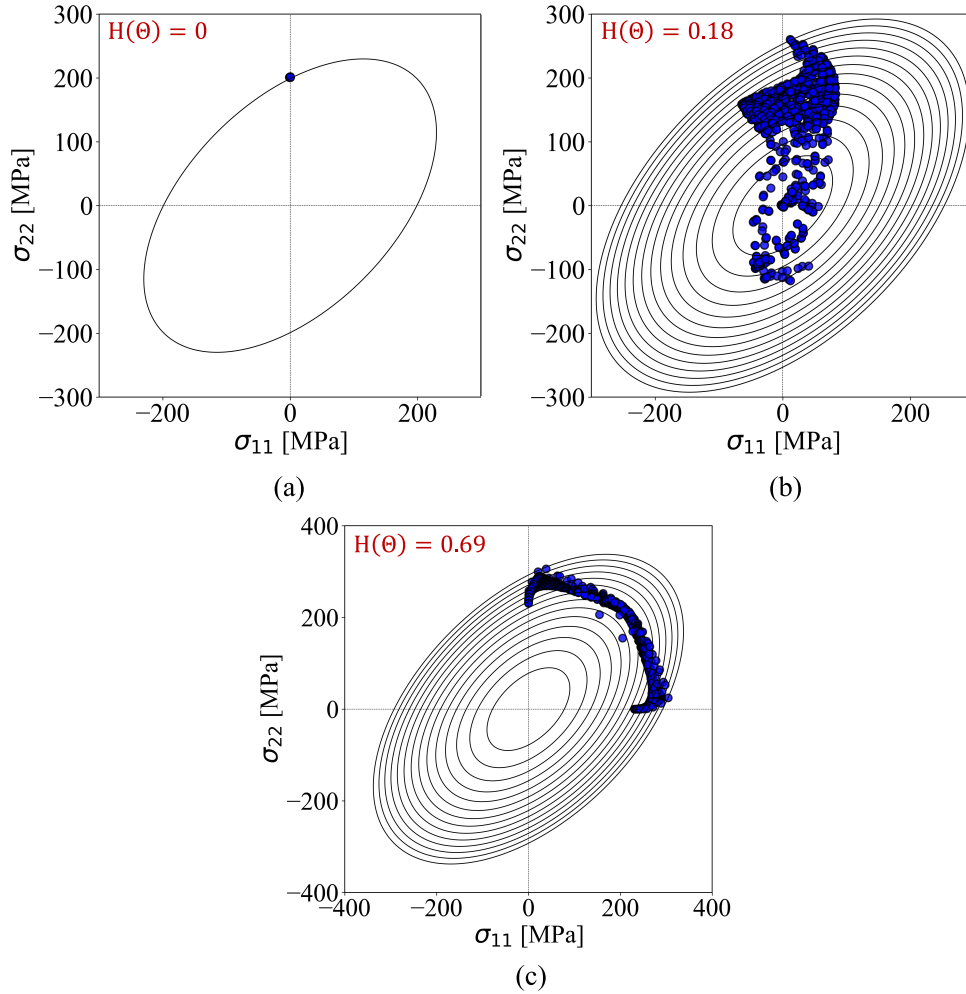


Figure 3: Stress distributions on the  $\sigma_{11}$  and  $\sigma_{22}$  yield loci, annotated with stress state entropy values for the (a) uniaxial tension specimen, (b)  $\Sigma$ -shaped specimen, and (c) cruciform specimen.

To offer further qualitative insights into the stress state richness, Figure 4 illustrates the locations of the generated stress states of each specimen on the 2-D Lode angle parameter – stress triaxiality coordinate system. This depiction highlights the diversity,

or lack thereof, in the stress states generated by each of the considered test specimens.

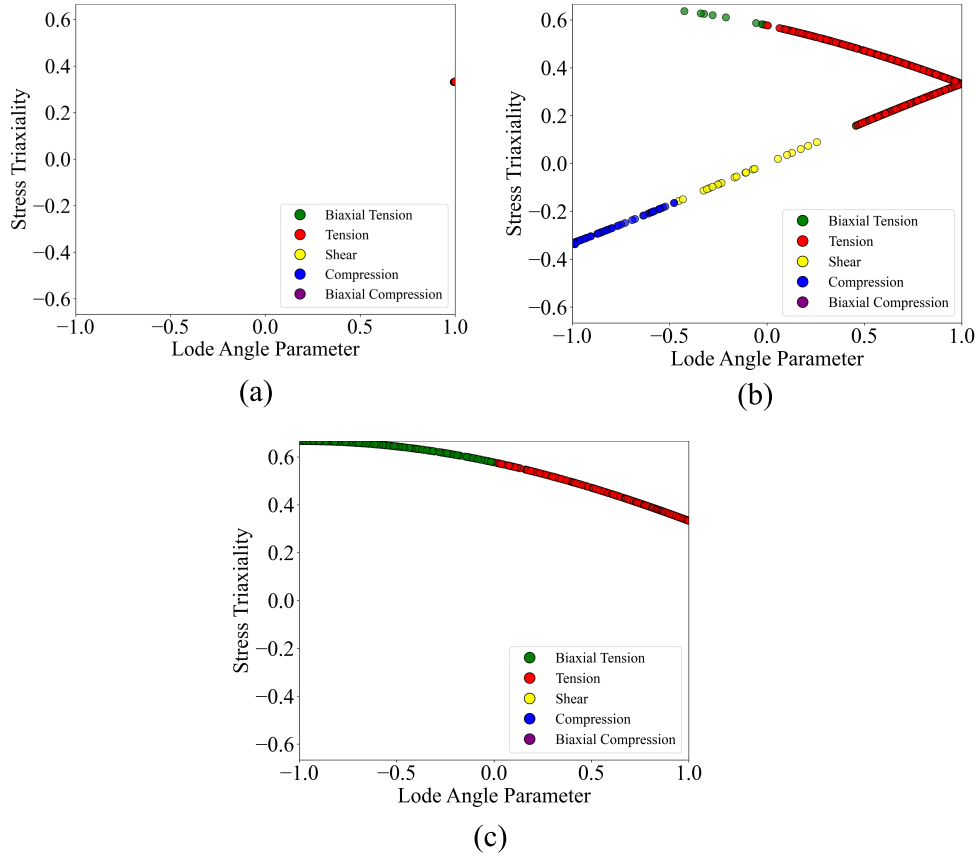


Figure 4: Stress state distributions on the 2-D Lode angle parameter – stress triaxiality coordinate system for the (a) uniaxial tension specimen, (b)  $\Sigma$ -shaped specimen, and (c) cruciform specimen.

From Figures 3a and 4a, the stress state generated by the uniaxial tension specimen is distinctly uniform, concentrated at a single point on the yield surface. This corresponds to a purely uniaxial tensile response along the RD, with a stress state entropy of  $H(\Theta) = 0$ . This entropy value indicates the specimen provides no information about the broader spectrum of stress states required to learn the material law accurately.

In contrast, the  $\Sigma$ -shaped specimen demonstrates a significantly more diverse stress state distribution, as evidenced by its complex profile on the yield surface (Fig. 3b). Mapping this distribution in the 2D Lode angle parameter – stress triaxiality space (Fig. 4b) reveals a combination of tension-dominant, compression-dominant, and shear states. The enhanced information content is quantified by a stress state entropy of  $H(\Theta) = 0.18$ , highlighting the specimen's capability to capture a wider range of stress states relevant to the stress space under consideration. Nevertheless, the tensile stress state along the RD remains the predominant feature, limiting the overall stress state entropy value.

Lastly, the cruciform specimen generates stress states characterized by uniaxial tension in its arms and biaxial tension near its center. This specimen geometry effectively captures the uniaxial tensile response along both the RD and the TD. As a result, the stress state entropy for the cruciform specimen is markedly higher, with  $H(\Theta) = 0.69$ . Which is the maximum stress state entropy for a stress state space with cardinality  $n = 2$ . This high entropy value reflects the specimen’s capability to represent tensile stress states in the RD and TD with equal distributions. However, despite its comprehensive coverage of tensile states, the cruciform specimen provides no information on shear stress states, limiting its utility in fully exploring the stress space under consideration.

#### 4.4. Parameter identification

The three test specimens are evaluated for their effectiveness in inversely learning the anisotropic inelastic material law. To learn the material law, six parameters, ( $A$ ,  $\varepsilon_0$ ,  $n$ ,  $F$ ,  $G$ , and  $N$ ), are to be identified. An attempt is made to simultaneously identify all parameters from the strain fields generated by each geometry. For consistency, the optimization process begins with the same initial parameter set across all test cases. The resulting identified parameters, along with the absolute error for each parameter, are presented in Table 1, highlighting the distinct contributions of each specimen’s information content to the accuracy of parameter identification.

Table 1: Identified parameter sets for the three specimen geometries

	$A$ [MPa]	$\varepsilon_0$	$n$	$F$	$G$	$N$
Ground truth	471.92	0.0098	0.29	0.278	0.373	2.340
Uniaxial tension specimen	451.92	0.0096	0.20	0.207	0.508	3.506
Absolute error (%)	4.11	2.01	31.03	25.54	36.19	49.83
$\Sigma$ -shaped specimen	470.66	0.00888	0.205	0.385	0.372	2.346
Absolute error (%)	0.14	9.39	29.31	38.50	0.27	0.26
Cruciform specimen	480	0.0085	0.245	0.283	0.376	2.748
Absolute error (%)	1.85	13.27	15.52	1.79	0.80	17.44

For all cases, convergence to the global minimum is achieved within approximately 75 iterations (Fig.A1). Furthermore, Figures A2, A3, and A4 present a visual comparison between the ground truth strain fields and those reconstructed using the identified parameters for all three specimens. The agreement between the ground truth and reconstructed strain fields shows the effectiveness of the optimization procedure in minimizing

the objective function. However, as shown in Table 1, the accuracy of the identified material law parameters varies across specimens. This discrepancy arises because no single specimen provides sufficient information to accurately identify all material parameters.

To further evaluate how closely the identified parameters reflect the material law, we analyze the predicted yield surface and yield stress anisotropy in Figure 5. Figures 5a and 5b depict the first quadrant of the symmetric yield surface in the  $\sigma_{11}$ - $\sigma_{22}$  and  $\sigma_{22}$ - $\tau_{12}$  planes, respectively, comparing the ground truth yield surface with the yield surfaces predicted using the identified parameters. Additionally, Figure 5c illustrates the evolution of the normalized yield stress as a function of the angle of orientation from the RD. The yield stresses obtained using the ground truth parameters are compared against those predicted using the identified parameters.

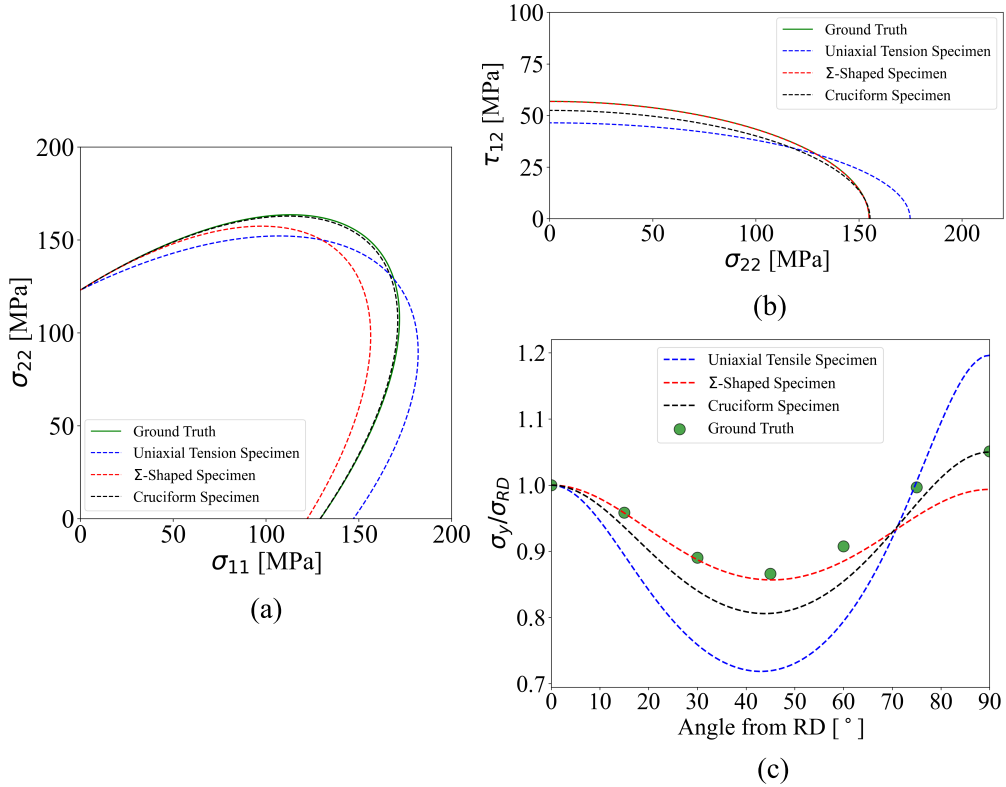


Figure 5: Comparison of the ground truth and identified anisotropic yield response in key stress planes: (a)  $\sigma_{11}$ - $\sigma_{22}$  plane, (b)  $\sigma_{22}$ - $\tau_{12}$  plane, and (c) normalized yield stress as a function of the orientation angle relative to the rolling direction (RD).

The results reveal that the uniaxial tension specimen’s limited stress state information, essentially confined to simple tension along the RD, restricts its effectiveness in accurately learning the material law. As this specimen does not generate a sufficiently informative data set to fully constrain the optimization, parameter adjustments com-

pensate to approximate the ground truth data as closely as possible. Consequently, all material parameters, except for the hardening parameters ( $A$  and  $\varepsilon_0$ ), are identified with large errors. This limitation is evident in the discrepancies observed between the predicted and ground truth yield surfaces (Figures 5a and 5b). As a result, the identified parameters fail to accurately learn the hardening behavior and yield stress anisotropy. While the predicted yield surface along the RD and the normalized yield stress at the RD ( $0^\circ$ ) align well with the ground truth value (Figure 5c), the variation in yield stress across different angles of orientation is poorly represented. These findings in parameter identification are consistent with those of (Pottier et al., 2011), which emphasize the necessity of incorporating data from uniaxial tensile test specimens oriented along the RD, TD, and at a  $45^\circ$  angle to adequately capture such a material law. In essence, enhancing the information content of the data through multiple tests.

As the information content of the test specimen increases, the material parameters become progressively decoupled, revealing their sensitivity to the complexity of strain fields associated with specific stress states. The  $\Sigma$ -shaped specimen provides stress state information relevant to both uniaxial tension in the RD and shear. This additional information imposes constraints on the optimization process, enabling accurate identification of the parameters  $G$  and  $N$ , which govern the inelastic uniaxial response in the RD and the shear response, respectively. This accuracy is reflected in the agreement between the predicted and ground truth yield surfaces in the  $\sigma_{22}$ - $\tau_{12}$  plane, as well as the close alignment of normalized yield stresses across orientations from  $0^\circ$  to  $60^\circ$ . However, the limited stress state information for uniaxial tension in the TD led to inaccuracies in identifying the parameter  $F$ . This error resulted in poor agreement with the yield surface in the  $\sigma_{11}$ - $\sigma_{22}$  plane and in the normalized yield stress predictions as the orientation angle approached  $90^\circ$ . Additionally, the data from this specimen was insufficient to fully decouple all parameters, leaving some of the hardening parameters ( $\varepsilon_0$  and  $n$ ) inaccurately identified. To accurately learn the material law using the  $\Sigma$ -shaped specimen, a combination of tests is also required. As demonstrated by (Kim et al., 2014), combining two tests with  $\Sigma$ -shaped specimens oriented in the RD and TD is necessary for overcoming its limited tensile stress information in the TD for accurately learning the material law.

Lastly, the cruciform specimen generates uniaxial stress states in both the RD and TD, enabling the accurate identification of the parameters  $F$  and  $G$ , which govern the



material’s inelastic tensile response in the RD and TD, respectively. The accuracy of these predictions is evident in the close alignment between the predicted and ground truth yield surfaces in the  $\sigma_{11}$ – $\sigma_{22}$  plane, as well as in the normalized yield stress predictions at the  $0^\circ$  and  $90^\circ$  orientations. However, the absence of shear stress state information in this specimen limits its accuracy in identifying the parameter  $N$ . This limitation is reflected in the poor agreement between the predicted and ground truth yield surfaces in the  $\sigma_{22}$ – $\tau_{12}$  plane, as well as in the under-prediction of normalized yield stresses at orientations between  $0^\circ$  and  $90^\circ$ , where the shear response plays a significant role. Also, since the cruciform specimen does not generate all required stress states to fully decouple the material parameters, the hardening parameters ( $\varepsilon_0$  and  $n$ ) were identified with errors. This outcome is consistent with the findings of (Martins et al., 2019), which suggest that a modified cruciform specimen capable of generating shear stress response is necessary for accurately learning the material law.

These results highlight the crucial role of stress state information in accurately learning material laws. Specimens capable of generating multiple stress states, such as the  $\Sigma$ -shaped and cruciform specimens, provide richer datasets that enable the accurate identification of certain material law parameters. The diversity of stress state information in the data effectively constrains the optimization process, reducing parameter coupling and improving prediction accuracy. However, none of the test specimens examined provided information on the stress states ( $\Theta = \{\sigma_{UT}^{RD}, \sigma_{UT}^{TD}, \sigma_S\}$ ) required accurately learn the material law in a single test. This raises an essential question: *”How can we enhance the information content of our test data to accurately learn the constitutive material law?”*. Two potential strategies emerge. The first approach involves integrating data from multiple tests conducted under varied loading states to ensure a diverse range of stress conditions. Alternatively, a single test could be designed to achieve an optimal stress state entropy, maximizing the information richness for parameter identification. In this work, we will focus on implementing the second strategy.

## 5. Informative specimen design

The preliminary attempts to learn the material law using a single test raised a crucial question: *”How can we enhance the information content of our test data to accurately learn the constitutive material law?”*. To address this challenge, we propose a method-

ology that incorporates stress state entropy as an objective function within a Bayesian optimization (BO) framework for designing test specimens. This approach facilitates the inverse design of specimen geometries by optimizing the stress state entropy. Thus, we can enrich the data available for accurately learning the material law. The biaxial cruciform specimen (Fig. 2c) serves as the base geometry for the inverse design, as it generates two of the three stress states required and has the highest stress state entropy among the current candidates ( $H(\Theta) = 0.69$ ).

The optimization process utilizes the Tree-Structured Parzen Estimator (TPE) algorithm (Bergstra et al., 2011), to optimally introduce and modify geometric features in the base geometry to achieve the stress state entropy requirement. TPE is chosen for its ability to perform an informed and adaptive search for optimal parameters, leveraging insights from previously evaluated parameter configurations to select new promising configurations. The parameter space  $\mathbf{P} = \{x_i, y_i, r_i\}$  is explored, where  $x_i$  and  $y_i$  define the positions of geometric inclusions, and  $r_i$  represents the radius of any notches or holes introduced. To increase the information content of the designed specimen, the design process is formulated as:

$$\mathbf{P}^* = \arg \max_{\mathbf{P}} H(\Theta). \quad (30)$$

Additionally, the BO framework employs Sequential Model-Based Global Optimization (SMBO) as an iterative method. SMBO initializes by building a probability model for the objective function and identifies locally optimal parameters through an acquisition function. This function guides the search by striking a balance between the *exploration* of the search space and the *exploitation* of promising regions in the search space. The expected improvement (EI) is used as the acquisition function, defined as:

$$\text{EI}_{(H^*)}(\mathbf{P}) = \int_{-\infty}^{H^*} (H^* - H)p(H | \mathbf{P}) dH, \quad (31)$$

where  $H^*$  is a threshold entropy. Given the parameter space  $\mathbf{P}$ , EI is the expectation that  $H$  will exceed  $H^*$ . Furthermore, TPE uses Bayes' theorem to decompose  $p(H | \mathbf{P})$  into  $p(\mathbf{P} | H)$  and  $p(\mathbf{P})$  in the form:

$$p(H | \mathbf{P}) = \frac{p(\mathbf{P} | H)p(H)}{p(\mathbf{P})}, \quad (32)$$

$$p(\mathbf{P} | H) = \begin{cases} l(\mathbf{P}), & H < H^* \\ g(\mathbf{P}), & H \geq H^* \end{cases}, \quad (33)$$

where  $l(\mathbf{P})$  is a Gaussian Mixture Model (GMM) fitted by the TPE to the set of parameter values associated with the best objective values, and  $g(\mathbf{P})$  is another GMM constructed simultaneously using the remaining parameter values.

The algorithm was integrated into a comprehensive framework that couples the optimization scheme with ABAQUS<sup>®</sup> FE software. The FE software was responsible for generating the specimen model given the parameters from the BO algorithm, applying the mesh and the necessary boundary conditions, running the simulation, and outputting the stress field. The stress field is then discretized to evaluate the stress state entropy values at each iteration. The optimization process demonstrated high efficiency, consistently generating a posterior parameter distribution for specimen geometries with optimal stress state entropy (Eq. 28) within 200 iterations.

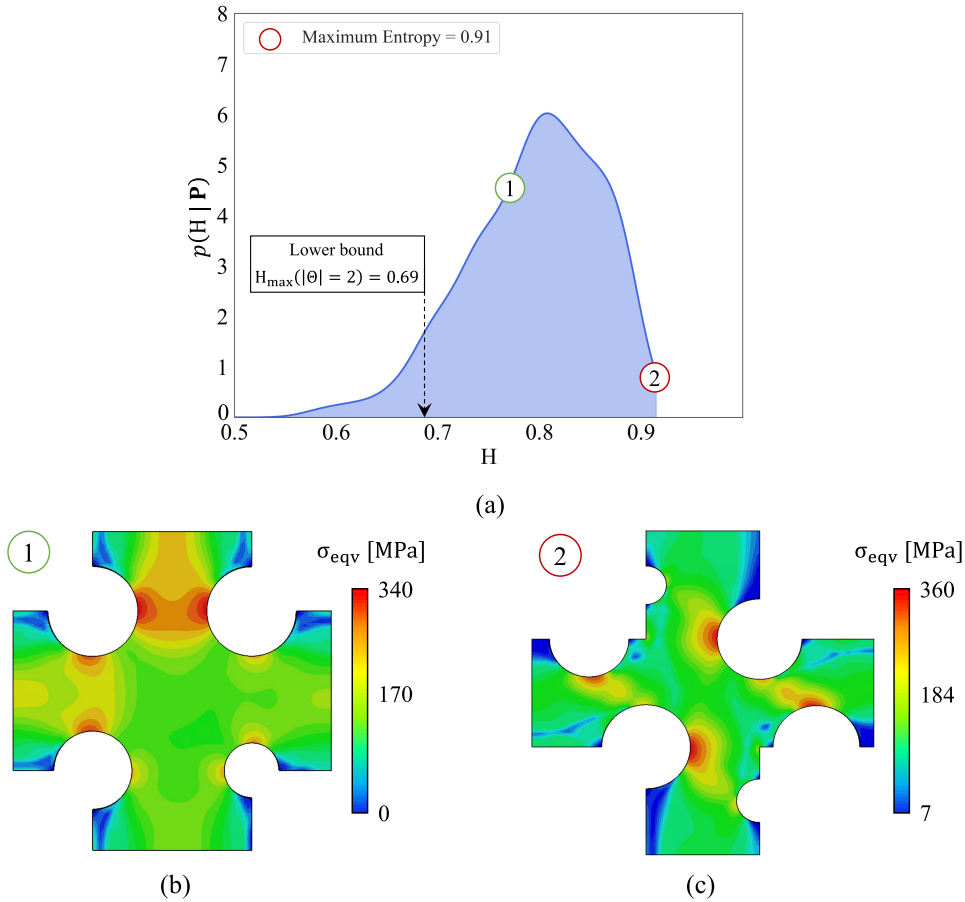


Figure 6: Informative specimen design: (a) Posterior density of the inverse design space, highlighting two sampled points (1 and 2) with stress state entropy values of 0.78 and 0.91 bits, respectively. The resulting specimen geometries from the sampled points, showing their equivalent stress fields: (b) Cruciform 1 and (c) Cruciform 2.

Figure 6a illustrates the posterior distribution of the stress state entropy given the

geometric parameter vector, where each point in the distribution represents a uniquely designed geometry defined by a specific parameter set and its associated stress state entropy. The majority of the designed geometries exhibited entropy values of 0.81, with the maximum stress state entropy for a designed geometry reaching 0.91. Additionally, Figure 6b and Figure 6c highlights the two geometries sampled at points 1 and 2 (beyond the lower bound of the maximum entropy hypothesis) with respective stress state entropy values of 0.78 and 0.91 bits. These specimens are selected to assess their stress state information content, viability for learning the material law, and to verify the optimal entropy hypothesis (Eq. 28). Notably, despite the difference in their entropy values, both specimens fall within the hypothesized optimal entropy range. Detailed geometric dimensions for these high-entropy, optimized specimens are shown illustrated in Figure B1.

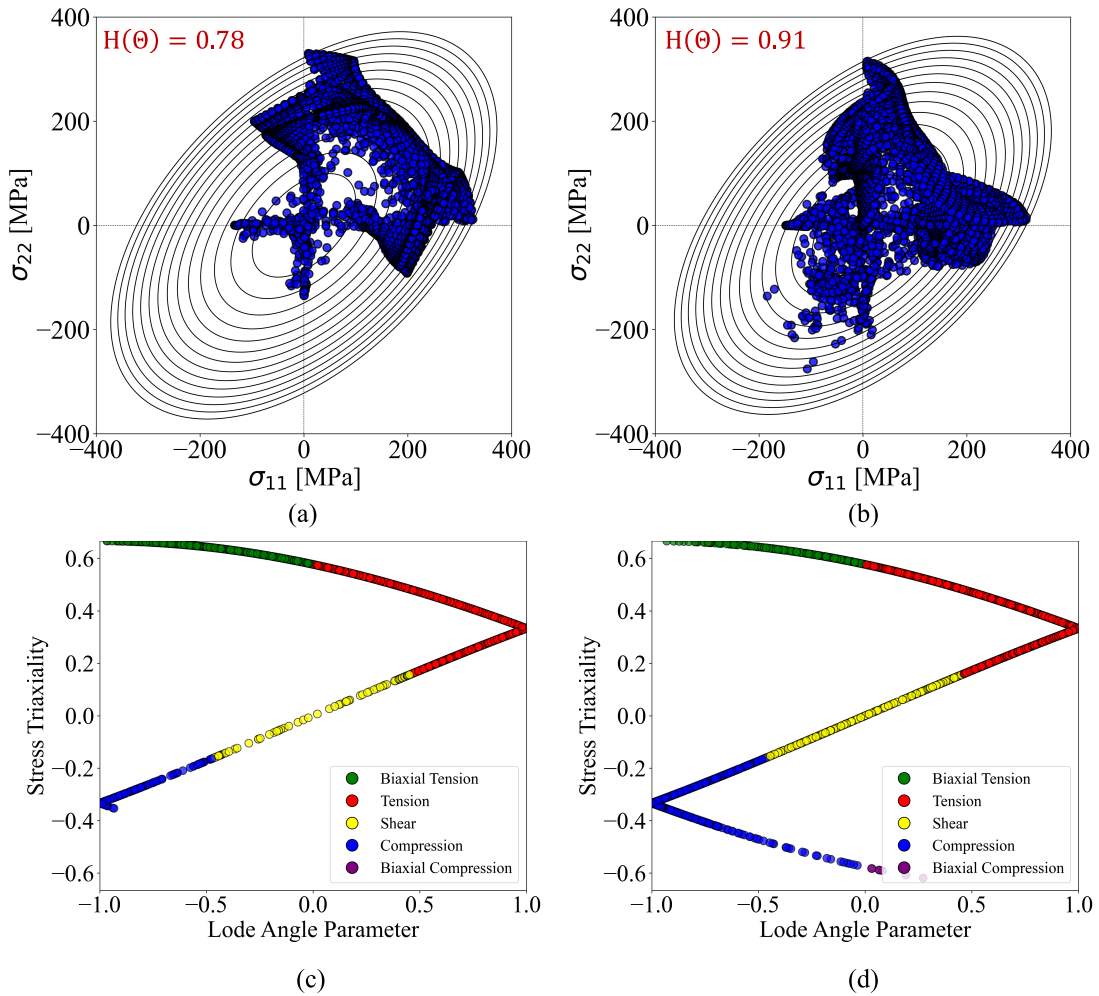


Figure 7: Stress distributions on the  $\sigma_{11}$  and  $\sigma_{22}$  yield loci, annotated with stress state entropy values for (a) cruciform 1 and (b) cruciform 2. Stress state distribution on the 2-D Lode angle parameter—stress triaxiality coordinate system for (c) cruciform 1 and (d) cruciform 2.

Figure 7 gives a qualitative illustration of the stress state information of the optimized specimens, which exhibit increased stress state entropy compared to the uniaxial tension,  $\Sigma$ -shaped, and cruciform specimens. In Figures 7a and 7b, the stress distributions along the  $\sigma_{11}$ - $\sigma_{22}$  yield loci for the optimized specimens reveal a broader coverage of the yield surface. Furthermore, their enhanced stress state entropy is evident in the 2-D Lode angle parameter – stress triaxiality space, as shown in Figures 7c and 7d.

From Figure 7, it is evident that the optimized specimens generate a diverse range of stress states, including uniaxial tension along the RD, biaxial tension compensating for the TD, and shear. Hence, the optimized specimens provide sufficient stress state information for accurately learning the material law. Although not considered in our stress state space, the test specimens also show compressive stress state information. The difference in the stress state entropy between the specimens is also qualitatively evident in Figure 7, where the specimen with higher entropy exhibits a broader distribution of stress states, both across the yield surface and within the 2-D Lode angle parameter – stress triaxiality space.

## 6. Performance of informative specimen in inverse learning

Here, we evaluate the optimized cruciform specimens for their effectiveness in accurately learning the material law. Additionally, to assess the robustness of these specimens under realistic testing conditions, Gaussian white noise,  $\mathcal{N}(\mu = 0, \sigma^2)$ , is added to the experimental strain fields at two distinct levels. The first noise level, with a standard deviation of  $\sigma = 10^{-3}$ , represents the typical uncertainty observed in carefully conducted large strain measurements (Sutton et al., 2009). The second noise level, characterized by a standard deviation of  $\sigma = 5 \times 10^{-3}$ , represents an elevated noise scenario, enabling a rigorous evaluation of specimen performance under challenging experimental conditions. Table 2 provides a summary of the material parameters identified across these cases.

Table 2: Identified parameter sets for the optimized specimen geometries

	$\mathcal{N}(0, \sigma^2)$	$A$ [MPa]	$\varepsilon_0$	$n$	$F$	$G$	$N$
Ground truth	-	471.92	0.0098	0.29	0.278	0.373	2.340
Cruciform 1	Noise-free	455.14	0.00891	0.284	0.280	0.374	2.325
	Absolute error (%)	3.43	9.08	2.07	0.72	0.27	0.64
	$\mathcal{N}(0, (10^{-3})^2)$	450.63	0.00895	0.287	0.278	0.375	2.337
	Absolute error (%)	4.38	8.67	1.03	0.00	0.54	0.13
	$\mathcal{N}(0, (5 \times 10^{-3})^2)$	465.95	0.00883	0.286	0.277	0.372	2.350
	Absolute error (%)	1.13	9.89	1.38	0.36	0.27	0.43
Cruciform 2	Noise-free	466.02	0.0087	0.280	0.279	0.371	2.353
	Absolute error (%)	1.12	11.22	3.45	0.26	0.62	0.55
	$\mathcal{N}(0, (10^{-3})^2)$	459.67	0.0086	0.280	0.292	0.373	2.361
	Absolute error (%)	2.46	12.24	3.45	5.04	0.00	0.89
	$\mathcal{N}(0, (5 \times 10^{-3})^2)$	461.52	0.0086	0.281	0.269	0.371	2.338
	Absolute error (%)	2.07	12.24	3.10	3.24	0.54	0.09

The results demonstrate that the optimized test specimens generate sufficient stress state information for accurate parameter identification. The model parameters are all identified with minimal errors, as summarized in Table 2. Notably, the performance of test specimens with stress state entropy within the optimal range verifies the optimal entropy hypothesis. As long as the stress state entropy of the test specimen falls within the bounds defined by Equation 28, accurate parameter identification is achievable.

To visualize the accuracy of the identified parameters and their robustness to experimental noise, Figure 8 compares ground truth and predicted force–displacement response in the RD and TD, reconstructed from the identified parameters for the noise-free case. Additionally, Figures 9a and 9b, along with Figures 10a and 10b, provide a detailed comparison between the identified and ground truth yield surfaces. Lastly, the evolution of the normalized yield stress as a function of the orientation angle relative to the RD is presented in Figures 9c and 10c. These results demonstrate that the identified parameters accurately capture the yield stress evolution and the shape of the yield surface.

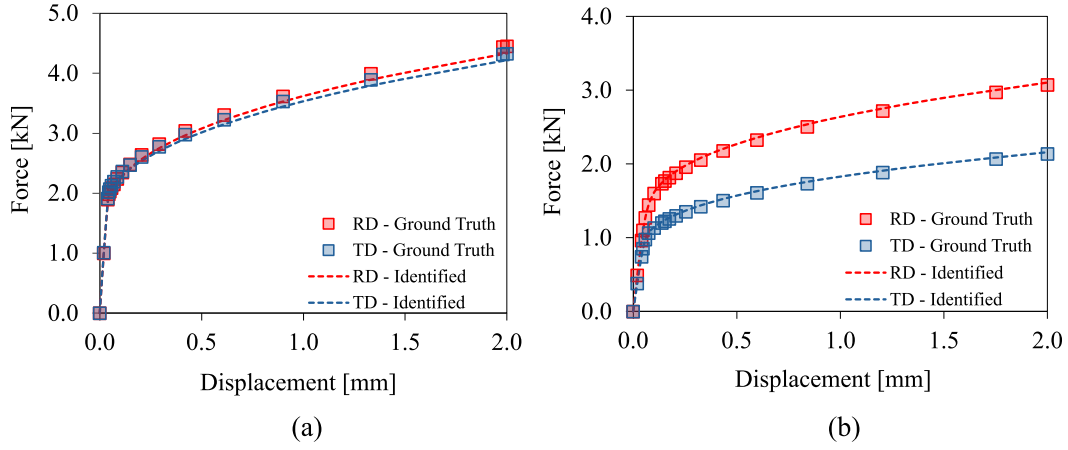


Figure 8: Comparison of the ground truth and identified force–displacement responses in the rolling direction (RD) and transverse direction (TD) for the optimally designed specimens: (a) Cruciform 1 and (b) Cruciform 2.

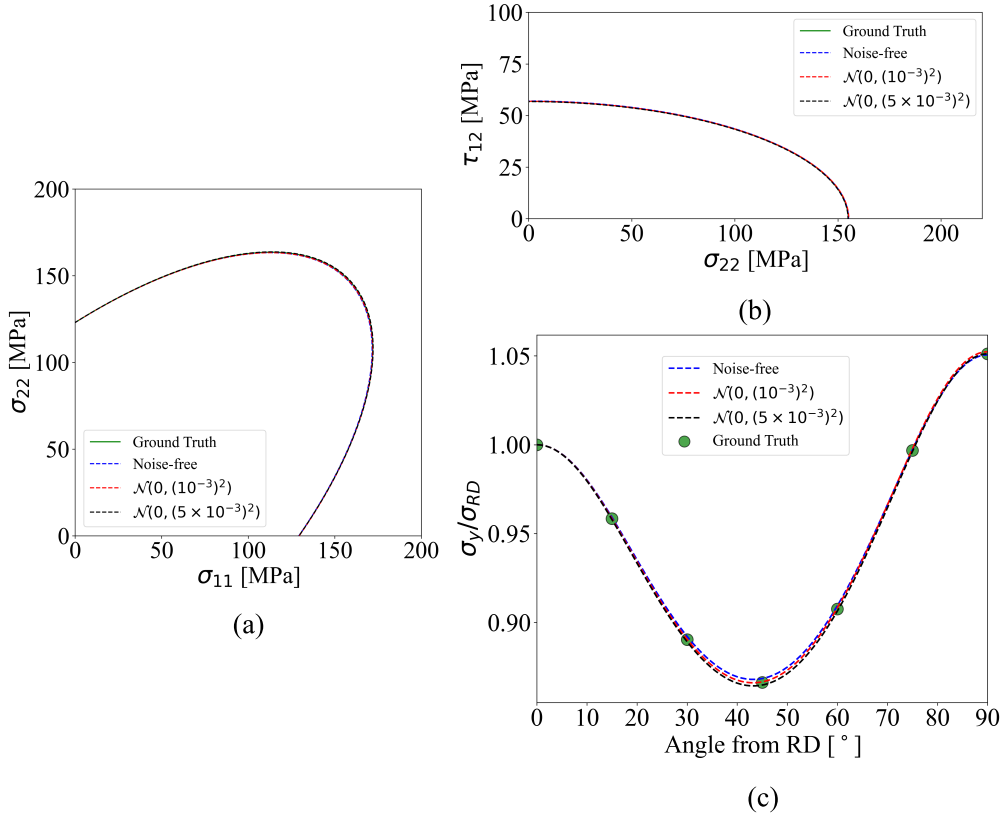


Figure 9: Comparison between the ground truth and identified anisotropic yield response in key stress planes for the optimally designed Cruciform 1: (a) yield contours in the  $\sigma_{11}$ – $\sigma_{22}$  plane, (b) yield contours in the  $\sigma_{22}$ – $\tau_{12}$  plane, and (c) normalized yield stress as a function of the orientation angle relative to the rolling direction (RD).

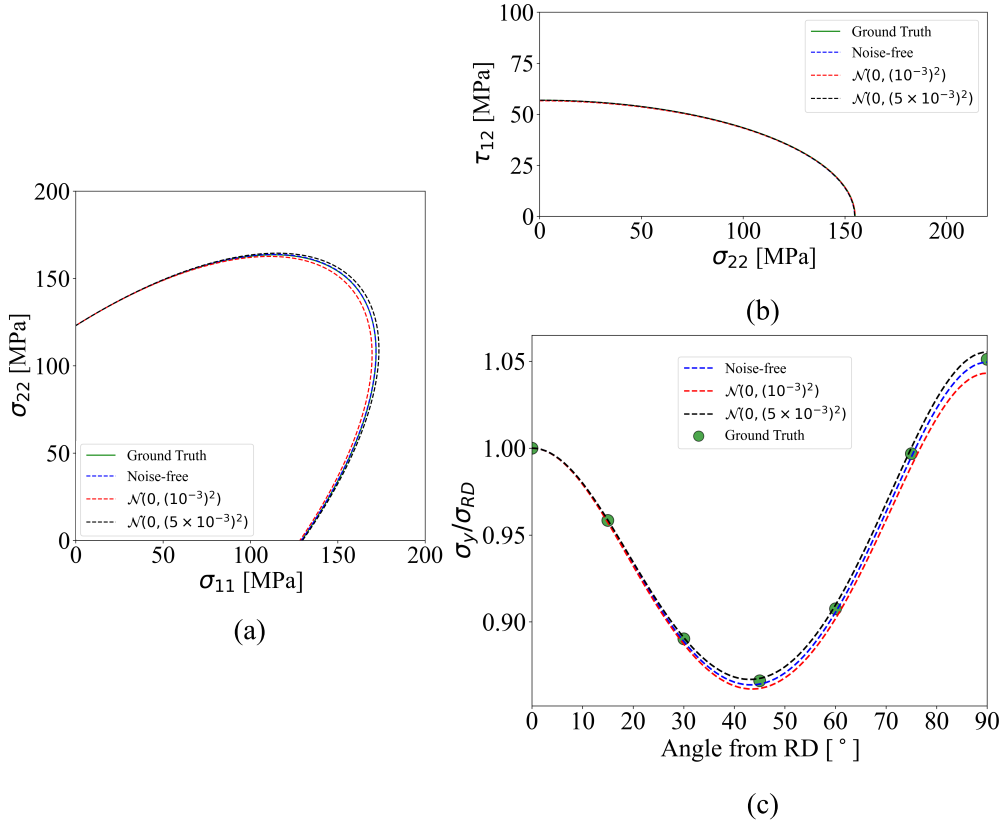


Figure 10: Comparison between the ground truth and identified anisotropic yield response in key stress planes for the optimally designed Cruciform 2: (a) yield contours in the  $\sigma_{11}$ - $\sigma_{22}$  plane, (b) yield contours in the  $\sigma_{22}$ - $\tau_{12}$  plane, and (c) normalized yield stress as a function of the orientation angle relative to the rolling direction (RD).

The results reveal that parameter identification using the optimally designed specimens is largely robust to the considered experimental noise levels. However, an interesting trend emerges: among the test specimens, Cruciform 2 with higher stress state entropy demonstrates greater sensitivity to noise. This observation is expected, as specimens with more informative data, while providing richer point-to-point information content, are inherently more vulnerable to experimental noise. This delicate trade-off between maximizing the information content and maintaining robustness to experimental uncertainties highlights a crucial consideration in test specimen design. It emphasizes the need to balance data richness with robustness to noise in the context of inverse learning and uncertainty quantification.



## 7. Uncertainty quantification

Uncertainty Quantification (UQ) is essential for ensuring both accuracy and reliability in inverse learning, particularly when employing geometrically complex and highly informative test specimens. Although these specimens generate informative data, due to their geometric complexities, they often introduce measurement uncertainties. This is especially true when using full-field techniques such as DIC, and quantifying such uncertainties is generally ignored in the deterministic parameter identification framework. Here, we leverage Bayesian UQ to rigorously quantify the aleatoric uncertainty associated with the full-field data. We also assume that the model fully captures the material behavior, thus excluding epistemic uncertainty. By establishing credible intervals for the identified parameters, this approach assesses the effect of experimental noise on parameter estimation. The Bayesian framework enables us to infer credible bounds in the parameter space, providing a robust framework for inverse learning and evaluating the robustness of test data in the presence of uncertainties.

In the Bayesian inverse learning framework, the model parameters are treated as random variables, denoted by  $\boldsymbol{\theta}$ . These parameters are assumed to follow independent prior distributions, each characterized by a probability density function,  $p(\boldsymbol{\theta})$ . The primary objective of this approach is to identify the parameters governing the material behavior while rigorously accounting for uncertainties inherent in the experimental data. This goal is achieved by updating the prior knowledge of the parameters through the incorporation of observed data and can be formally expressed as:

$$\mathbf{y} = \mathcal{G}(\boldsymbol{\theta}) + \mathcal{N}, \quad (34)$$

where  $\mathbf{y}$  represents the full-field experimental data,  $\mathcal{G}(\boldsymbol{\theta})$  is the forward operator or model, and  $\mathcal{N}$  represents the uncertainty in the data. Applying Bayes' theorem to update the parameter distribution  $\boldsymbol{\theta}$  is fundamental to the framework, and it is expressed as:

$$p(\boldsymbol{\theta} | \mathbf{y}) = \frac{p(\mathbf{y} | \boldsymbol{\theta}) \cdot p(\boldsymbol{\theta})}{p(\mathbf{y})}. \quad (35)$$

The probability density function for the prior distribution  $p(\boldsymbol{\theta})$  of the model parameters can either be informative or uninformative, depending on the level of confidence in the available prior knowledge regarding the parameter distribution. The prior distribution encodes the assumptions or knowledge about the parameters before any data is

observed, thus influencing the posterior parameter estimates. In cases where limited or no prior knowledge is available, an uninformative prior is typically used. A uniform distribution is often adopted as the uninformative prior, as it represents a state of complete uncertainty about the parameters. In this study, we select a uniform distribution as the prior, expressed as:

$$p(\boldsymbol{\theta}) = \prod_{i=1}^n \frac{1}{b_i - a_i}, \quad (36)$$

where  $n$  denotes the total number of parameters, and  $a_i$  and  $b_i$  represent the lower and upper bounds of the  $i$ -th parameter, respectively. Furthermore, derived from Equation 35, the term  $p(\mathbf{y} | \boldsymbol{\theta})$  corresponds to the likelihood, which quantifies the probability of observing the data  $\mathbf{y}$  given the model predictions parameterized by  $\boldsymbol{\theta}$ . The likelihood is modeled as a Gaussian process, which provides a probabilistic measure of model–data agreement. For computational efficiency, and exploiting the monotonicity of the logarithmic function, the likelihood is expressed in logarithmic form as:

$$\ln p(\mathbf{y} | \boldsymbol{\theta}) = -\frac{n}{2} \ln(2\pi) - \frac{1}{2} \ln |\boldsymbol{\Sigma}| - \frac{1}{2} \sum_{i=1}^n (\mathbf{y}_i - \mathcal{G}_i(\boldsymbol{\theta}))^T \boldsymbol{\Sigma}^{-1} (\mathbf{y}_i - \mathcal{G}_i(\boldsymbol{\theta})), \quad (37)$$

where  $\boldsymbol{\Sigma}$  is the diagonal covariance matrix that captures the aleatoric uncertainty in the data,  $\mathcal{G}_i(\boldsymbol{\theta})$  represents the model prediction corresponding to the  $i$ -th experimental observation  $\mathbf{y}_i$  for the parameter set  $\boldsymbol{\theta}$ ,  $n$  is the total number of experimental data points, and the superscript T indicates the transpose operation.

The final term in Equation 35,  $p(\mathbf{y})$  is the model evidence, also known as the marginal likelihood, which serves as a normalizing factor to ensure that the posterior distribution is a valid probability distribution. The evidence is expressed as:

$$p(\mathbf{y}) = \int p(\mathbf{y} | \boldsymbol{\theta}) p(\boldsymbol{\theta}) d\boldsymbol{\theta}. \quad (38)$$

When the posterior distribution  $p(\boldsymbol{\theta} | \mathbf{y})$  is high-dimensional and/or exhibits significant complexity, the marginal likelihood  $p(\mathbf{y})$  becomes intractable and lacks a closed-form solution. Hence, approximate approaches are required to determine the posterior distribution. Typically, sampling techniques are employed to evaluate the posterior distribution indirectly, circumventing the direct computation of the marginal likelihood. Specifically, Markov Chain Monte Carlo (MCMC) methods (Robert, 1999) are utilized to construct a Markov chain whose stationary distribution corresponds to the target posterior distribution. In this study, the random walk MCMC method is employed, wherein samples

are iteratively drawn from a Gaussian proposal distribution. The acceptance of each proposed sample is determined using the Metropolis-Hastings (MH) criterion,  $\alpha$ , defined as:

$$\alpha(\boldsymbol{\theta}^{(i-1)}, \boldsymbol{\theta}^{(*)}) = \min \left\{ 1, \frac{p(\boldsymbol{\theta}^{(*)} | \mathbf{y})}{p(\boldsymbol{\theta}^{(i-1)} | \mathbf{y})} \cdot \frac{q(\boldsymbol{\theta}^{(*)}, \boldsymbol{\theta}^{(i-1)})}{q(\boldsymbol{\theta}^{(i-1)}, \boldsymbol{\theta}^{(*)})} \right\}, \quad (39)$$

where  $\boldsymbol{\theta}^{(i-1)}$  represents the current state of the chain,  $\boldsymbol{\theta}^{(*)}$  is the proposed state, and  $q$  is the proposal distribution. In this work, the proposal distribution is Gaussian, facilitating efficient exploration of the parameter space.

This framework is applied to perform UQ in learning the material law using the optimally designed specimens, incorporating a noise level of  $\mathcal{N}(0, (10^{-3})^2)$  in the experimental data. The results, shown in Figure 11 illustrate the 90% credible interval uncertainty bounds, showing the impact of experimental noise on inverse learning using the optimized test specimens.

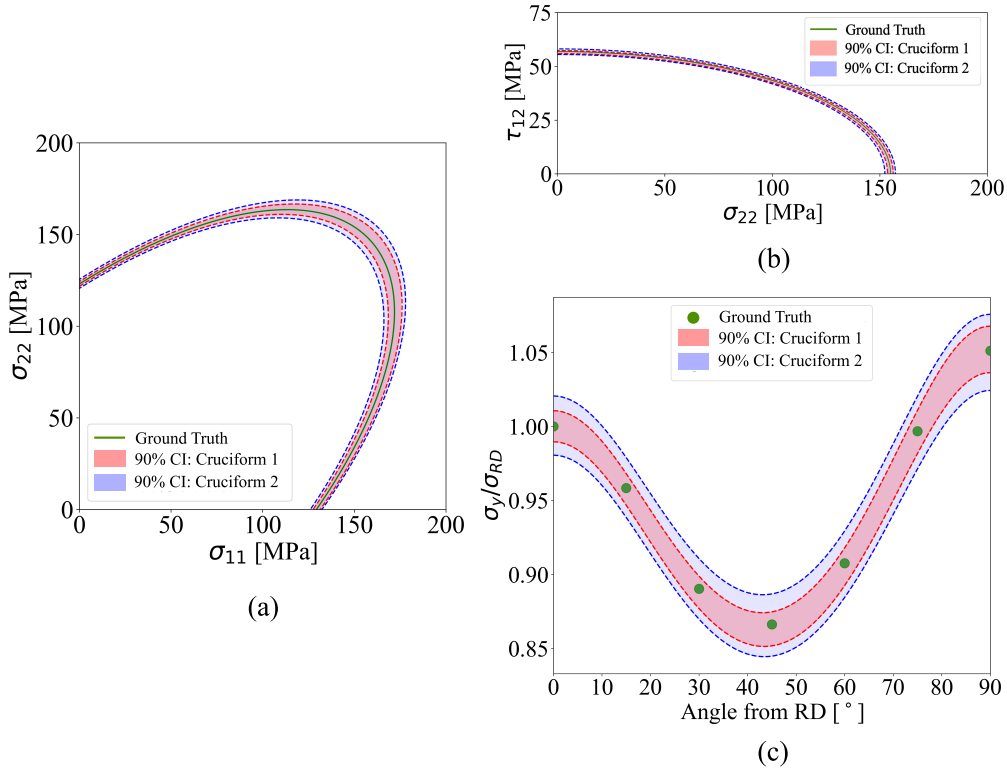


Figure 11: Yield surface reconstruction from noisy test data for Cruciform 1 and Cruciform 2, incorporating uncertainty quantification with 90% credible interval bounds across key stress planes: (a)  $\sigma_{22}$ - $\sigma_{11}$  plane, (b)  $\sigma_{11}$ - $\tau_{12}$  plane, and (c) normalized yield stress as a function of the orientation angle relative to the rolling direction (RD).

The results presented in Figure 11 demonstrate that the optimized specimens exhibit robustness to the prescribed noise level, as evidenced by the distribution of the con-

confidence bounds around the ground truth. Notably, Cruciform 2, characterized by the highest stress state entropy ( $H(\Theta) = 1.32$  bits), exhibits a broader CI, reflecting greater uncertainties in learning the material law under noisy conditions. This observation is consistent with findings from the deterministic framework, which showed that specimens with higher stress state entropy, are less robust to experimental noise. These results highlight the trade-off between maximizing the information content of the test data and ensuring robustness to experimental uncertainties.

## 8. Discussions

### 8.1. Efficiency vs. robustness in learning constitutive models

In contrast to the conventional human-centered learning paradigm, which heavily relies on a multi-experiment approach, the proposed informatics-driven framework offers significant advantages in learning efficiency. First, it eliminates the necessity for maintaining a pure stress state in the specimen, thereby eliminating the need for costly specimen optimization, control, and refinement. While an informative specimen is ideal, the framework does not impose strict requirements on specimen geometry, affording greater flexibility in the selection of testing equipment and fixtures. Second, the framework significantly reduces the number of required tests. The examples presented in this study demonstrate that a 6-parameter, 2D material model can be learned accurately using data from a single test. Third, the learning process has the potential to be fully automated, minimizing the need for user expertise and intervention. Collectively, these advantages directly address the limitations discussed in Section 1.

Despite its advantages, it is unlikely that the proposed informatics-led framework will completely replace the conventional human-centered learning paradigm. The primary reason is the robustness of the conventional approach, which allows for identifying parameters associated with a single stress state from a single test. Although specimens in this paradigm carry limited information, resulting in a stress state entropy close to zero, all material points in the specimen convey the same information. This makes measurements simpler and more cost-effective because the process is more resilient to missing data or significant noise in localized regions, as measurements can still be reliable.

In contrast, the new informatics-driven framework relies on a single, highly informative test to calibrate multiple parameters, necessitating full-field measurements. This

requirement renders the framework more sensitive to missing data or localized experimental noise which is common in DIC measurements of strain and displacement fields (Rossi et al., 2015; Rossi and Pierron, 2012). Figure 12 illustrates the impact of these issues on learning accuracy using the optimized Cruciform 2. In Case 1, one-third of the data points are randomly missing, while in Case 2, a localized region of the specimen experiences an amplified characteristic noise level of  $\mathcal{N}(0, (0.5)^2)$ . As shown, the resulting uncertainty in the learning process is significantly amplified, underscoring the sensitivity of the framework to data quality and completeness.

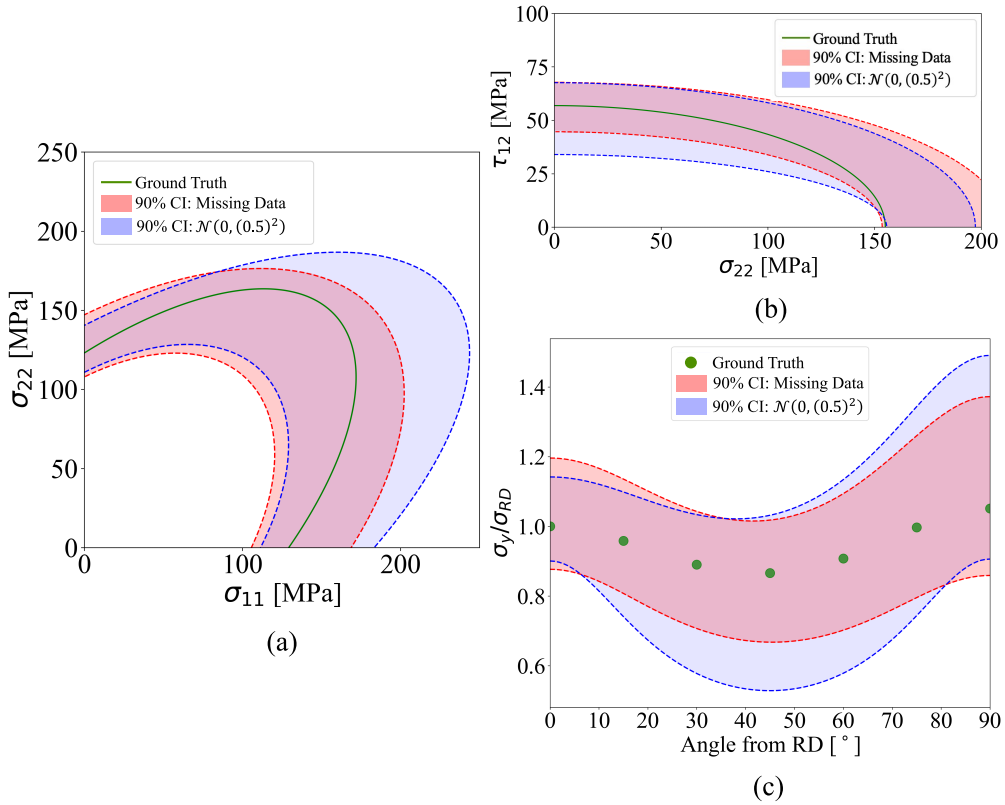


Figure 12: Yield surface reconstruction from Cruciform 2 test data accounting for the impact of missing data and severe localized noise in uncertainty quantification with 90% credible interval bounds across key stress planes: (a)  $\sigma_{11}$ - $\sigma_{22}$  plane, (b)  $\sigma_{22}$ - $\tau_{12}$  plane, and (c) normalized yield stress as a function of the orientation angle relative to the rolling direction (RD).

In summary, the process of learning constitutive models from experimental data inherently balances efficiency and robustness. State-of-the-art approaches often integrate elements of both paradigms to optimize performance. As experimental and computational techniques continue to evolve, achieving greater robustness and reliability, this trade-off is expected to shift progressively toward increased efficiency. Such advancements hold the potential to enable a more autonomous learning process.

## 8.2. The least informative specimen

In the informatics-led inverse learning framework, it is evident that specimens providing more information can facilitate the learning of a greater number of parameters. Therefore, finding the "most informative" specimen becomes a priority to enhance learning efficiency. However, in many practical scenarios, the "least informative" specimen is preferred, especially when robustness is a key consideration in traditional human-centered learning approaches. A notable example is the experimental determination of fracture strain, where maintaining a constant stress state throughout the test is essential.

The experimental uncertainties associated with determining strain to fracture under a pure stress state have driven the development of strategies aimed at designing specimens that maintain such conditions within a defined gage section of a specimen approaching failure. Traditionally, these designs rely on trial-and-error approaches (Peirs et al., 2012) or parametric studies of specimen geometries in attempts to ensure a constant stress state up to failure (Roth and Mohr, 2016, 2018). In this study, we demonstrate that stress state entropy offers a robust alternative, serving as an objective function for designing test specimens with uniform information content across the gage area.

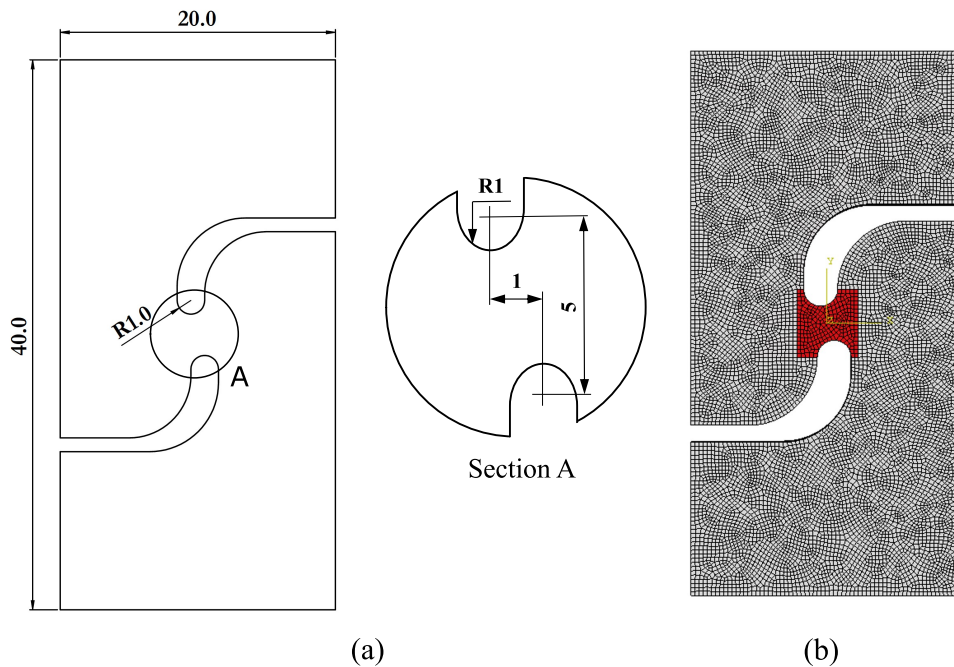


Figure 13: Shear specimen: (a) Geometry of the base specimen (Peirs et al., 2012), and (b) finite element model illustrating the mesh and highlighting the critical gage region.

As a case study, we focus on the optimal design of the Peirs' (Peirs et al., 2012) shear test specimen (Fig. 13) to maintain a pure shear stress state under large deformations in

its gage section. Despite extensive numerical and experimental efforts (Roth and Mohr, 2018; Peirs et al., 2012), achieving a consistent pure shear stress state in the specimen’s critical gage region throughout its loading history has proven challenging. To ensure a constant pure stress state while accounting for the inelastic material behavior, both the stress triaxiality ( $\eta$ ) and the Lode angle parameter ( $\bar{\theta}$ ) at the shear line or critical gage regions must maintain a value of 0 throughout the deformation process. The design problem is mathematically formulated as a multi-objective minimization problem in the form:

$$\mathbf{P}^* = \arg \min_{\mathbf{P}} (\bar{H}(\Theta), \bar{\eta}) . \quad (40)$$

Here,  $\mathbf{P}^*$  represents the vector space of geometric parameters that uniquely define the design of the specimen. The parameter space  $\mathbf{P} = \{x_i, y_i, R\}$  is explored, where  $x_i$  and  $y_i$  define the center location of notches, and  $R$  represents the notch radius, set to be the same for both notches. Also,  $\bar{H}(\Theta)$  and  $\bar{\eta}$  denote the average stress state entropy and stress triaxiality within the gage section of the specimen, respectively. The multi-objective optimization follows the BO framework detailed in Section 5. The objective functions are minimized sequentially. First, the stress state entropy is minimized to ensure that the average information content in the gage section is  $\bar{H}(\Theta) = 0$  bit. Subsequently, to achieve a pure shear stress state, the posterior distribution of the parameter space yielding this entropy is further refined to minimize the stress triaxiality. This approach defines a posterior distribution over the sampled design parameters that characterize the specimen geometry, ensuring a gage area with minimal information content and a pure stress state.

Following the specimen optimization framework, posterior distributions of the stress state entropy and the stress triaxiality are obtained. Figure 14a presents the joint posterior distribution of these quantities on a contour plot, highlighting three distinct points that correspond to unique locations within the  $(\bar{H}(\Theta), \bar{\eta})$  coordinate system. The geometries and equivalent plastic strain fields within the critical gage region of the specimens, designed based on the parameters associated with these locations, are shown in Figure 14b.

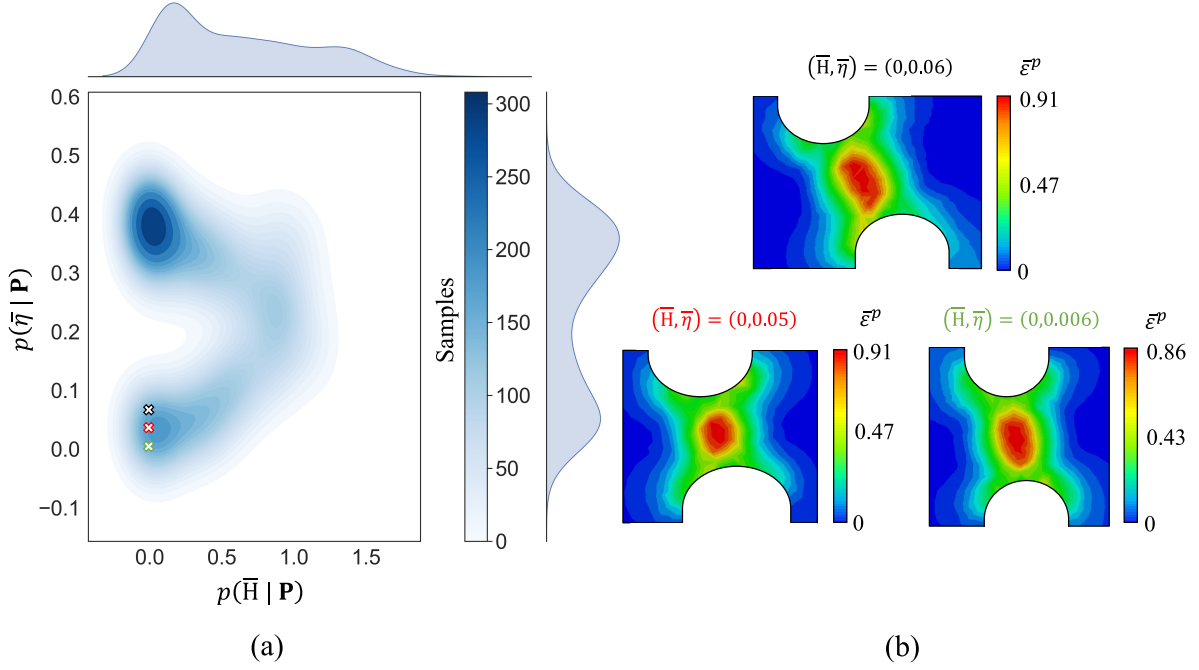


Figure 14: Specimen optimization results: (a) Joint distribution of posterior densities of the stress state entropy and stress triaxiality, and (b) geometry and equivalent plastic strain fields of sampled geometries from favorable regions in the  $(\bar{H}(\Theta), \bar{\eta})$  coordinate system.

Furthermore, an analysis of the loading paths for the critical element within the gage section of the sampled geometries (Fig. 14 b) reveals different behaviors. As shown in Figure 15, the geometries sampled at points  $(0, 0.06)$  and  $(0, 0.05)$  deviate from a pure shear state during their loading history. In contrast, the specimen corresponding to the location with minimal stress state entropy and stress triaxiality  $(0, 0.006)$ , maintains a pure shear stress state throughout its entire loading history. These results underscore the potential of the mechanics informatics paradigm in addressing challenges associated with determining strain to fracture under a pure stress state. By leveraging information-driven design, specimen geometries can be optimally tailored to ensure the required *pure stress state* is maintained throughout the entire loading history.



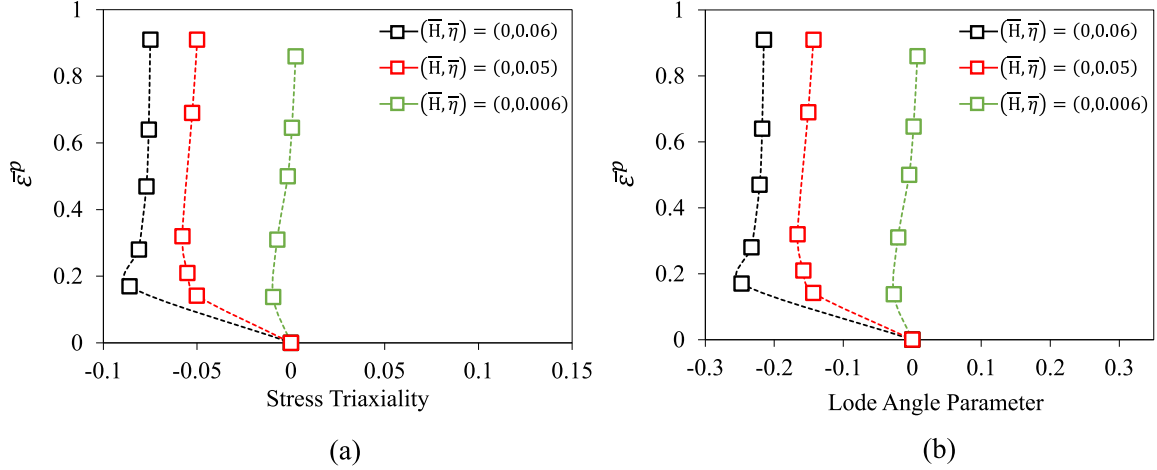


Figure 15: Loading paths for the critical element within the gauge section of the sampled geometries: (a) Evolution of the stress triaxiality with equivalent plastic strain, and the (b) evolution of the Lode angle parameter with equivalent plastic strain.

### 8.3. Transfer learning for inverse problems

Transfer learning, a powerful machine learning technique, involves re-purposing a model trained for one task as the foundation for solving a different but related task (Torrey and Shavlik, 2010). This strategy eliminates the need for extensive training from scratch, which typically demands large datasets and significant computational resources. Instead, it capitalizes on the knowledge embedded in a pre-trained model to improve learning efficiency and performance on the new task. Inspired by this paradigm, we pose a compelling question: if two distinct mechanical tests provide stress state information of comparable quantity and quality within the mechanics informatics framework, can they be utilized to infer the same material law? In other words, is the inverse learning process transferable across different mechanical tests?

In this study, we investigate the transferability of two distinct mechanical tests: equibiaxial tension and the mini-punch test, for learning material laws. Equibiaxial tension tests are a staple of traditional human-centered learning frameworks and typically rely on standard cruciform specimen geometries. However, performing equibiaxial tension tests presents significant challenges. The design of the loading fixture requires precise displacement control, while the fabrication of cruciform specimens demands meticulous considerations to ensure equibiaxial deformation at the center without premature failure in the arms. Due to these complexities, equibiaxial tension tests are often replaced by bulge or punch tests, where a thin sheet specimen is either deformed using hydraulic

pressure (Plancher et al., 2020) or by a spherical rigid punch (Zhu et al., 2014).

Figure 16 illustrates the geometries of the punch and specimen, highlighting the ROI and the FE model used for the mini-punch simulation. Notably, the central region in a mini-punch test achieves an ideal equibiaxial stress state, although deviations occur in the surrounding areas due to geometric constraints and frictional effects between the specimen and the punch (Zhang et al., 2017). Simulations involving the cruciform specimen were conducted as detailed in Subection 4.2. For the mini-punch test, the model consisted of a sheet metal specimen constrained by a pair of annular flanges with an inner diameter of 25 mm. Nodes located within a radial distance of 12.5 mm to 30 mm from the center were fully constrained. The punch was modeled as an analytical rigid shell with a radius of 6.35 mm and assigned a prescribed velocity of 0.033 mm/s in the z-direction. To minimize the influence of friction on the resulting strain field, a static coefficient of friction of 0.001 was employed. Symmetry boundary conditions were applied to the specimen geometry, enabling the simulations to be performed on a quarter of the specimen. This symmetry-based approach significantly reduced computational costs.

From the results, Figure 17 compares the stress distributions in the central regions of the two tests, on the  $\sigma_{11} - \sigma_{22}$  yield surface, as well as the distribution of the stress states on the Lode angle parameter – stress triaxiality coordinate system. The figure illustrates that both tests are qualitatively identical.

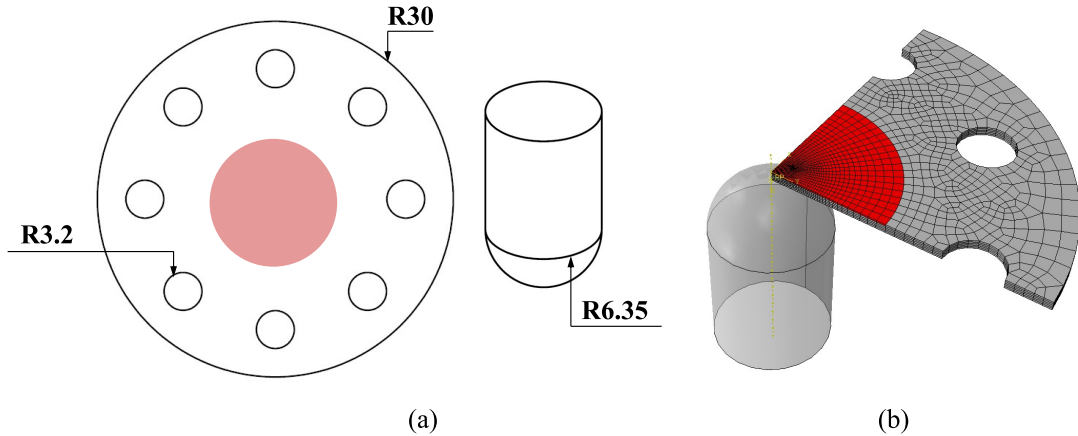


Figure 16: Mini-Punch Test: (a) Specimen geometry highlighting the region of interest, and (b) finite element model of a quarter of the specimen showcasing the refined mesh and the region of interest. All dimensions are in millimeters (mm)

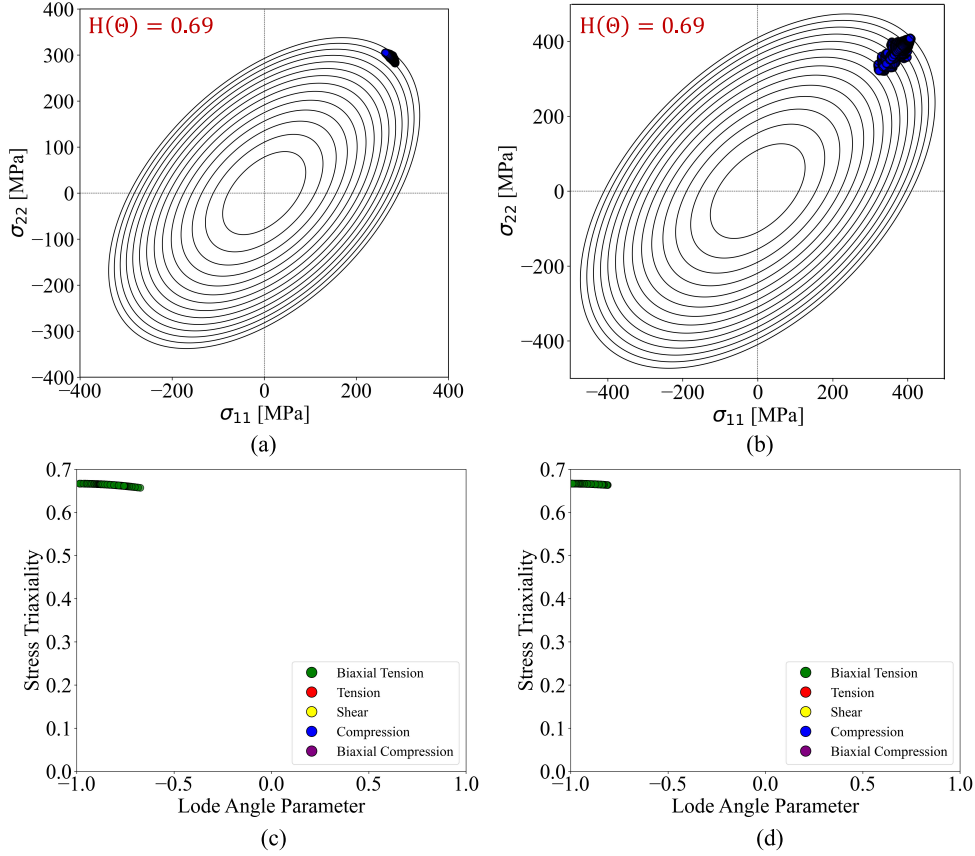


Figure 17: Stress distributions on the  $\sigma_{11}$  and  $\sigma_{22}$  yield loci, annotated with stress state entropy values for the (a) cruciform specimen and (b) mini-punch specimen. Stress state distribution on the 2-D Lode angle parameter—stress triaxiality coordinate system for (c) cruciform specimen and (d) mini-punch specimen.

Furthermore, given the material law and stress state space considered in this study ( $\Theta = \{\sigma_{UT}^{RD}, \sigma_{UT}^{TD}, \sigma_S\}$ ), an equibiaxial tensile stress state provides equivalent stress state information in tension along both the RD and TD. This equivalence implies that the stress state entropy of the ROI for both specimen geometries is identical, with a value of  $H(\Theta) = 0.69$ . This indicates that, in theory, the two tests are equivalent.

Using the test data generated from both specimens in inverse learning, and following the procedures outlined in Subsection 4.1, Table 3 summarizes the identified material law parameters obtained from the two specimens. Figure 18 compares the yield surfaces reconstructed from the ground truth with those predicted using the identified parameters. The results indicate that both specimens accurately identified parameters sensitive to the uniaxial tensile response in the RD and TD, which are well-represented by the specimens. This is evident from the good agreement in the yield surface in the  $\sigma_{11}$ - $\sigma_{22}$  plane (Fig. 18a) and the accurate prediction of the normalized yield stress at angles  $0^\circ$  and  $90^\circ$  from

the RD (Fig. 18c). However, the results also highlight the challenge of accurately learning the parameter associated with shear response ( $N$ ), as reflected in Figure 18c, where this stress state is absent in both specimens.

Table 3: Identified parameter sets for specimens with equivalent stress state information

	$A$ [MPa]	$\varepsilon_0$	$n$	$F$	$G$	$N$
Ground truth	471.92	0.0098	0.29	0.278	0.373	2.340
Cruciform specimen	471.11	0.0099	0.25	0.282	0.389	2.859
Absolute error (%)	0.04	1.02	13.79	1.44	4.29	22.18
Mini-Punch test	473.31	0.0085	0.285	0.288	0.378	2.659
Absolute error (%)	0.43	13.27	1.72	3.59	1.35	13.63

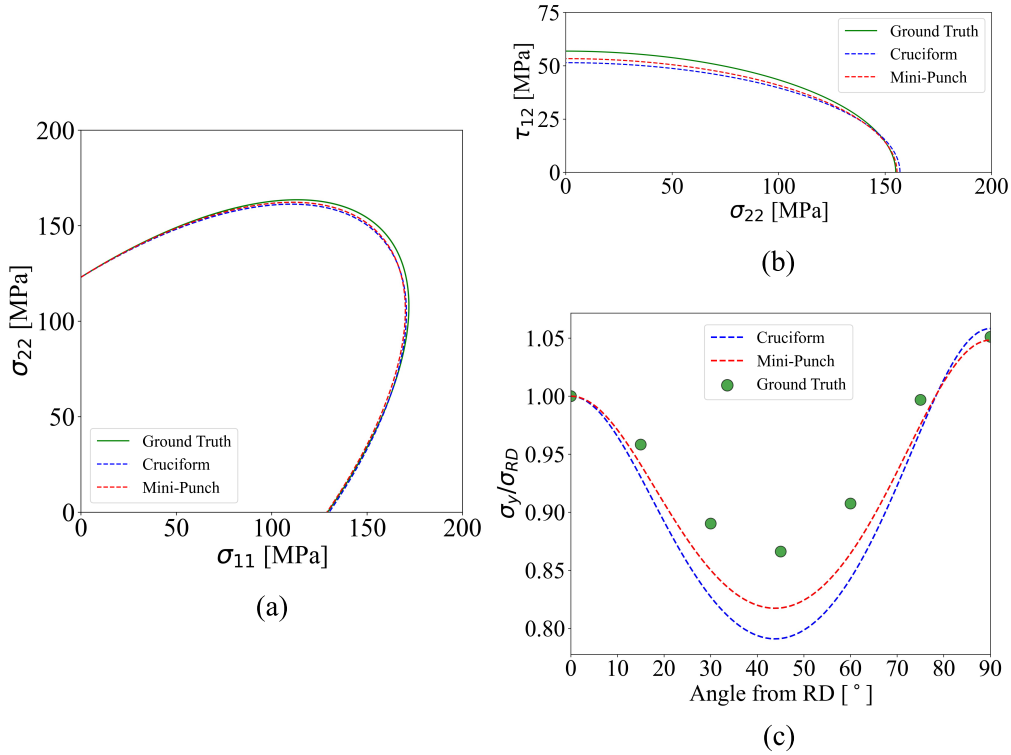


Figure 18: Comparison of the ground truth and identified anisotropic yield response in key stress planes for the cruciform and Mini-Punch tests: (a)  $\sigma_{11}$ - $\sigma_{22}$  plane, (b)  $\sigma_{22}$ - $\tau_{12}$  plane, and (c) normalized yield stress as a function of the orientation angle from the rolling direction (RD).

This example demonstrates the concept of *transfer learning* within the context of mechanics informatics. It offers practical relevance in experimental studies, where a challenging test can be substituted with a more feasible alternative that retains equivalent information content. In inverse learning, the unknown material parameters can still be accurately identified, ensuring reliable outcomes despite the test constraints.

## 9. Conclusions

This study introduces *Mechanics Informatics* as a paradigm for efficiently and accurately learning constitutive models, addressing fundamental challenges in quantifying the information content of mechanical test data. By introducing *stress state entropy* as a central metric, we have developed a framework for quantifying the information content of experimental data for efficiently and accurately learning constitutive models. We have explored the applicability of the uniaxial tension specimen,  $\Sigma$  – shaped specimen and cruciform specimen with different information content for accurately learning an anisotropic inelastic law in the Hill formulation. Notably, test specimens insufficient stress state information content partially constrained the optimization process, limiting accurate learning to only a few parameters strongly sensitive to the stress state information in the test data generated by the considered specimen.

The Mechanics Informatics paradigm was further extended to specimen design by incorporating stress state entropy within a Bayesian optimization scheme. In the first case, maximizing stress state entropy enabled the design of optimal cruciform specimens, which provided sufficient stress state information and ensured accurate parameter identification for the considered material law. The results also verified the optimal entropy criterion defined to bound the required stress state information for learning constitutive models between an upper and lower limit. Furthermore, our findings show that highly informative tests are susceptible to experimental uncertainties. and such uncertainties can amplify errors in the learning process. Hence, we highlight the trade-offs between maximizing the information content of the test data and ensuring robustness to uncertainties in experimental data. This emphasizes the need for high-quality, complete full-field data when using highly informative data in the informatics-driven workflow. In a contrasting specimen design case, the framework was applied to successfully minimise stress state entropy within the gage region of a Peirs shear specimen, achieving a pure shear stress state throughout the critical loading regime. The results show the flexibility of the mechanics informatics paradigm in enabling the targeted design of specimens for specific experimental goals, such as accurately determining strain-to-fracture under pure stress state conditions.

Finally, we demonstrated the potential of leveraging transfer learning within the mechanics informatics framework, providing a pathway for overcoming practical limitations

in experimental workflows. By efficiently learning material parameters using diverse test types that yield equivalent stress state information, we showcased the capability to adapt to constraints such as specimen design complexity or difficulties in precise displacement control. This adaptability reduces the dependency on exhaustive experimental testing while maintaining the fidelity required for accurate material parameter identification, thus streamlining computational and experimental workflows in constitutive model development.

In summary, this work introduces the Mechanics Informatics framework a paradigm for advancing accurate learning of constitutive models and experimental design. By developing a methodology to quantify the information content of test data, optimally design specimens in an information-driven manner, and address uncertainties, this paradigm offers a comprehensive toolkit for accurately learning constitutive models and enhancing the efficiency and reliability of experimental workflows.

### **CRedit authorship contribution statement**

Royal C. Ihuaenyi: Writing – original draft, Writing – review & editing, Visualization, Software, Methodology, Investigation, Formal analysis, Data curation, Conceptualization. Wei Li: Writing – review & editing, Software, Methodology. Martin Z. Bazant: Writing – review & editing, Supervision, Methodology, Conceptualization. Juner Zhu: Writing – original draft Writing – review & editing, Supervision, Resources, Project administration, Methodology, Investigation, Funding acquisition, Conceptualization.

### **Declaration of competing interest**

The authors declare that they have no known competing interests.

### **Acknowledgements**

The authors would like to thank Dr. Ruobing Bai for his constructive comments about the work.

### **Funding sources**

This work is supported by the startup fund for J.Z. from Northeastern University.

## Appendix A. Optimization descent and strain fields for the selected specimen geometries in inverse learning

Figure A1 depicts the optimization descent for the considered test specimen, with all cases showing convergence within 75 iterations. Furthermore, Figures A2, A3, and A4 illustrate the remarkable agreement between the reconstructed strain fields obtained from the identified parameters and those generated using the ground truth parameters for the considered specimen geometry. This consistency highlights the robustness of the proposed inverse learning framework in accurately identifying parameter sets that minimize the objective function.

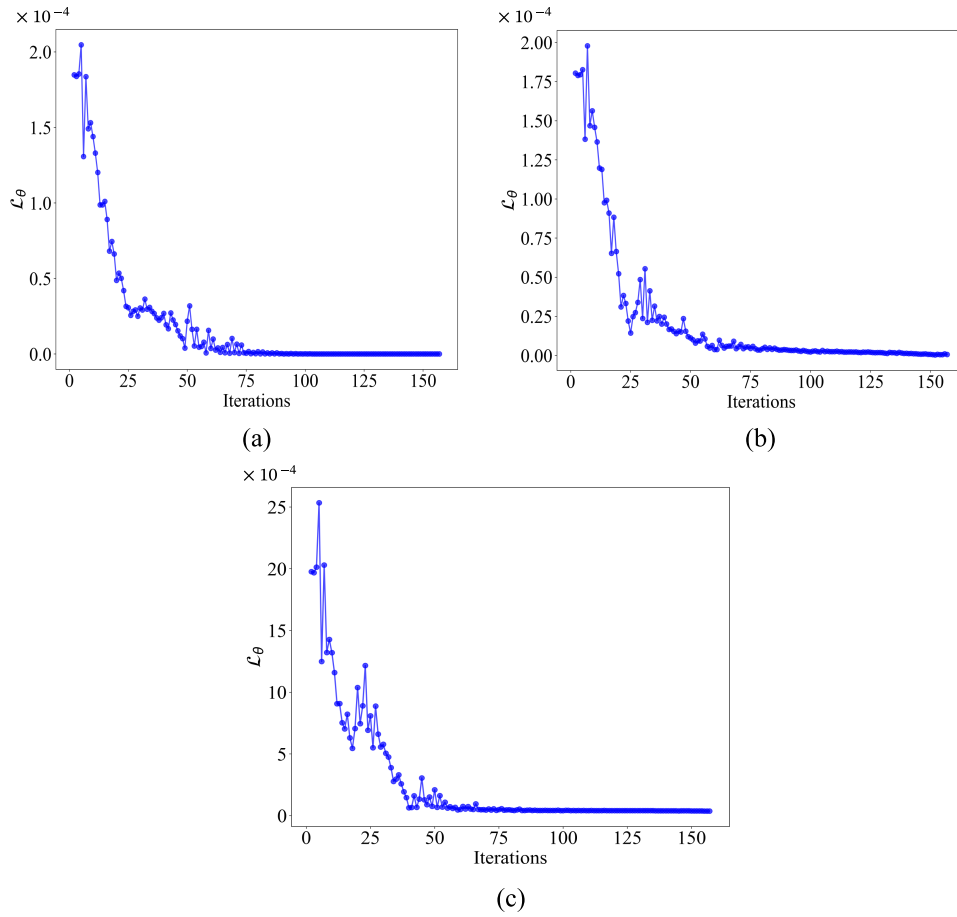


Figure A1: Evolution of the objective function with iterations for the (a) uniaxial tension specimen, (b)  $\Sigma$ -shaped specimen, and (c) cruciform specimen.

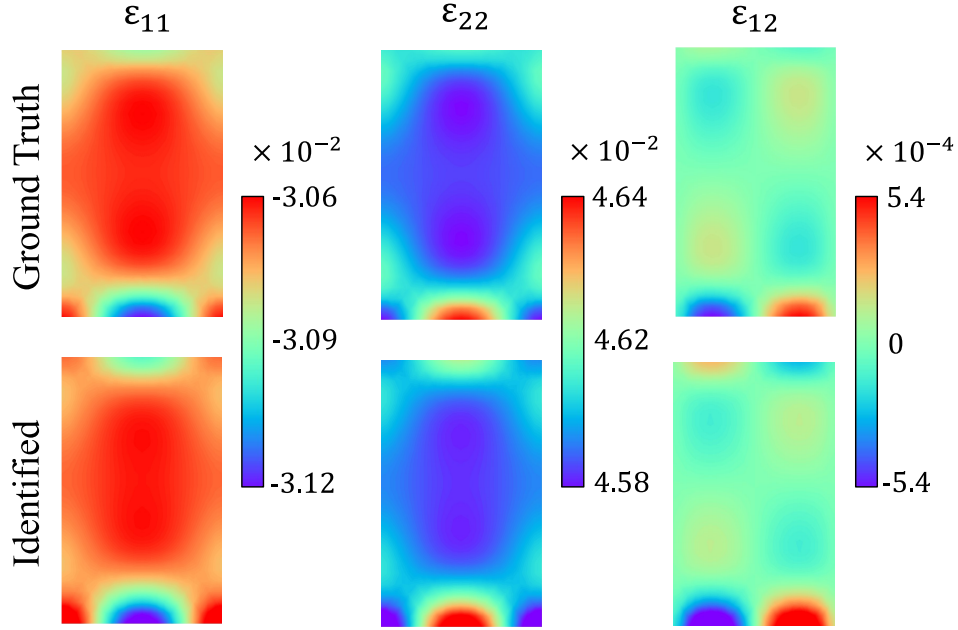


Figure A2: Comparison of strain fields for the region of interest (ROI) of the uniaxial tension specimen, illustrating the ground truth strain fields alongside the reconstructed strain fields derived from the identified parameters.

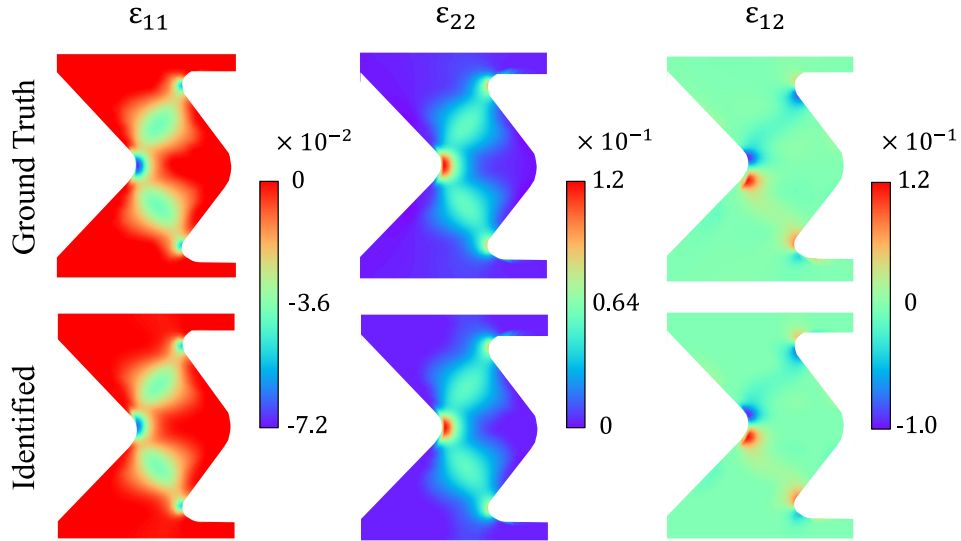


Figure A3: Comparison of strain fields for the region of interest (ROI) of the  $\Sigma$ -shaped specimen, illustrating the ground truth strain fields alongside the reconstructed strain fields derived from the identified parameters.



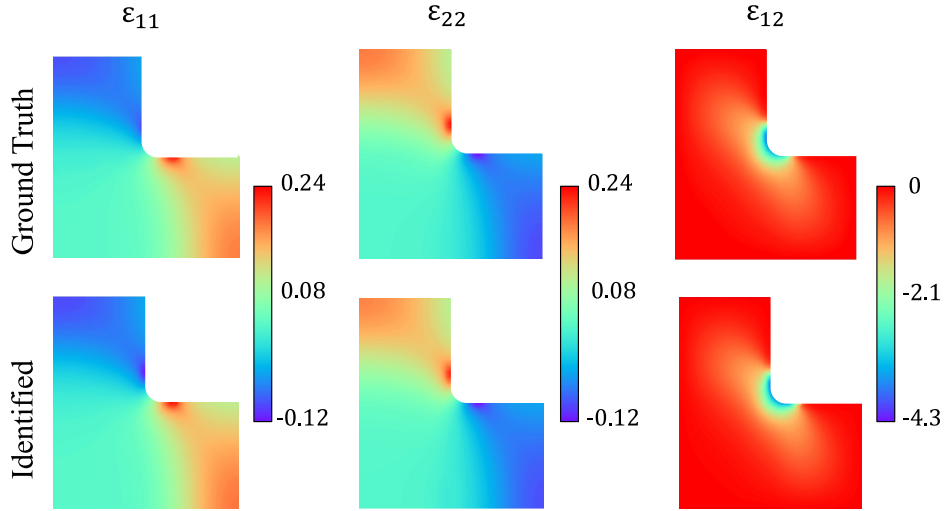


Figure A4: Comparison of strain fields for the region of interest (ROI) of the cruciform specimen, illustrating the ground truth strain fields alongside the reconstructed strain fields derived from the identified parameters.

## Appendix B. Optimally designed cruciform specimen geometries

Here, the geometries and dimensions of the optimally designed cruciform specimens are presented. These specimen geometries were designed to maximize the stress state information content in test data from a single experiment, enabling accurate and efficient learning of the considered constitutive model.

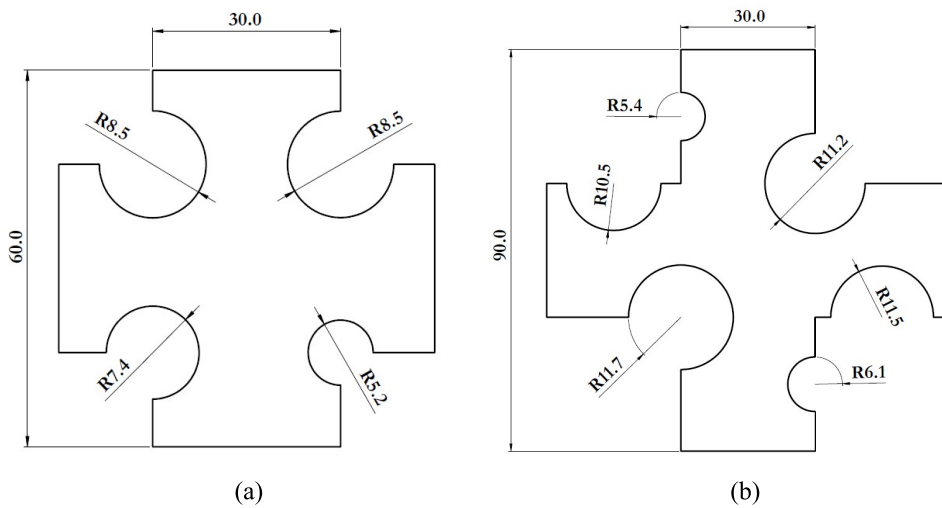


Figure B1: Geometric dimensions of the optimally designed cruciform specimens: (a) Cruciform 1 and (b) Cruciform 2. All dimensions are provided in millimeters (mm).

## Appendix C. Analytical formulation of the uniaxial tensile yield stress as a function of the orientation angle with respect to the rolling direction

The Hill48 anisotropic yield function under a plane stress assumption is expressed as:

$$2f(\boldsymbol{\sigma}) = F\sigma_{22}^2 + H(\sigma_{11} - \sigma_{22})^2 + G\sigma_{11}^2 + 2N\tau_{12}^2 = 1. \quad (\text{C.1})$$

By expanding and rearranging terms, Eq. C.1 can be reformulated as:

$$2f(\boldsymbol{\sigma}) = (G + H)\sigma_{11}^2 - 2H\sigma_{11}\sigma_{22} + (F + H)\sigma_{22}^2 + 2N\tau_{12}^2 = 1. \quad (\text{C.2})$$

For a uniaxial tensile specimen oriented at an angle  $\theta$  to the rolling direction, the stress components are related by:

$$\begin{cases} \sigma_{11} = \sigma_{\theta} \cos^2 \theta, \\ \sigma_{22} = \sigma_{\theta} \sin^2 \theta, \\ \tau_{12} = \sigma_{\theta} \sin \theta \cos \theta. \end{cases} \quad (\text{C.3})$$

Substituting Eq. C.3 into Eq. C.2, the uniaxial tensile yield stress  $\sigma_{\theta}$  is derived as:

$$\sigma_{\theta} = \frac{1}{\sqrt{F \sin^2 \theta + G \cos^2 \theta + H + (2N - F - G - 4H) \sin^2 \theta \cos^2 \theta}}. \quad (\text{C.4})$$

Equation C.4 provides the yield stress as a function of the orientation angle  $\theta$ , capturing the anisotropic nature of the material response.

### Data Availability

Data will be made available on request.

## References

- Alves, L.M., Nielsen, C.V., Martins, P.A., 2011. Revisiting the fundamentals and capabilities of the stack compression test. *Experimental Mechanics* 51, 1565–1572. doi:<https://doi.org/10.1007/s11340-011-9480-5>.
- Anghileri, M., Chirwa, E., Lanzi, L., Mentuccia, F., 2005. An inverse approach to identify the constitutive model parameters for crashworthiness modelling of composite structures. *Composite structures* 68, 65–74. doi:<https://doi.org/10.1016/j.compstruct.2004.03.001>.
- ASTM International, 2000. Standard test methods of compression testing of metallic materials at room temperature. ASTM International.
- Attia, P.M., Grover, A., Jin, N., Severson, K.A., Markov, T.M., Liao, Y.H., Chen, M.H., Cheong, B., Perkins, N., Yang, Z., et al., 2020. Closed-loop optimization of fast-charging protocols for batteries with machine learning. *Nature* 578, 397–402. doi:<https://doi.org/10.1038/s41586-020-1994-5>.
- Avril, S., Bonnet, M., Bretelle, A.S., Grédiac, M., Hild, F., Ienny, P., Latourte, F., Lemosse, D., Pagano, S., Pagnacco, E., Pierron, F., 2008a. Overview of identification methods of mechanical parameters based on full-field measurements. *Experimental Mechanics* 48, 381–402. doi:<https://doi.org/10.1007/s11340-008-9148-y>.
- Avril, S., Pierron, F., Sutton, M.A., Yan, J., 2008b. Identification of elasto-visco-plastic parameters and characterization of Lüders behavior using digital image correlation and the virtual fields method. *Mechanics of materials* 40, 729–742. doi:<https://doi.org/10.1016/j.mechmat.2008.03.007>.
- Aykol, M., Gopal, C.B., Anapolsky, A., Herring, P.K., van Vlijmen, B., Berliner, M.D., Bazant, M.Z., Braatz, R.D., Chueh, W.C., Storey, B.D., 2021. Perspective—combining physics and machine learning to predict battery lifetime. *Journal of The Electrochemical Society* 168, 030525. doi:[10.1149/1945-7111/abec55](https://doi.org/10.1149/1945-7111/abec55).
- Bao, Y., Wierzbicki, T., 2004. On fracture locus in the equivalent strain and stress triaxiality space. *International Journal of Mechanical Sciences* 46, 81–98. doi:[10.1016/j.ijmecsci.2004.02.006](https://doi.org/10.1016/j.ijmecsci.2004.02.006).

- Barroqueiro, B., Andrade-Campos, A., de Oliveira, J.D., Valente, R., 2020. Design of mechanical heterogeneous specimens using topology optimization. *International Journal of Mechanical Sciences* 181, 105764. doi:<https://doi.org/10.1016/j.ijmecsci.2020.105764>.
- Bergstra, J., Bardenet, R., Bengio, Y., Kégl, B., 2011. Algorithms for hyper-parameter optimization. *Advances in Neural Information Processing Systems* 24, 2546–2554.
- Cameron, B.C., Tasan, C.C., 2021. Full-field stress computation from measured deformation fields: A hyperbolic formulation. *Journal of the Mechanics and Physics of Solids* 147, 104186. doi:<https://doi.org/10.1016/j.jmps.2020.104186>.
- Cao, J., Bambach, M., Merklein, M., Mozaffar, M., Xue, T., 2024. Artificial intelligence in metal forming. *CIRP Annals* doi:<https://doi.org/10.1016/j.cirp.2024.04.102>.
- Cao, J., Banu, M., 2020. Opportunities and Challenges in Metal Forming for Lightweighting: Review and Future Work. *Journal of Manufacturing Science and Engineering* 142, 110813. doi:<https://doi.org/10.1115/1.4047732>.
- Carrara, P., De Lorenzis, L., Stainier, L., Ortiz, M., 2020. Data-driven fracture mechanics. *Computer Methods in Applied Mechanics and Engineering* 372, 113390. doi:[10.1016/j.cma.2020.113390](https://doi.org/10.1016/j.cma.2020.113390).
- Chang, C., Li, X., Xu, Z., Gao, H., 2017. Lithiation-enhanced charge transfer and sliding strength at the silicon-graphene interface: A first-principles study. *acta mechanica solida sinica* 30, 254–262. doi:<https://doi.org/10.1016/j.camss.2017.03.011>.
- Deng, H.D., Zhao, H., Jin, N., Hughes, L., Savitzky, B.H., Ophus, C., Fraggadakis, D., Borbély, A., Yu, Y.S., Lomeli, E.G., et al., 2022. Correlative image learning of chemo-mechanics in phase-transforming solids. *Nature Materials* 21, 547–554. doi:<https://doi.org/10.1038/s41563-021-01191-0>.
- Deng, N., Kuwabara, T., Korkolis, Y., 2015. Cruciform specimen design and verification for constitutive identification of anisotropic sheets. *Experimental Mechanics* 55, 1005–1022. doi:<https://doi.org/10.1007/s11340-015-9999-y>.

- Dreyer, C., Janotti, A., Van de Walle, C., 2015. Brittle fracture toughnesses of gan and aln from first-principles surface-energy calculations. *Applied Physics Letters* 106. doi:<https://doi.org/10.1063/1.4921855>.
- Dunand, M., Mohr, D., 2010. Hybrid experimental–numerical analysis of basic ductile fracture experiments for sheet metals. *International journal of solids and structures* 47, 1130–1143. doi:<https://doi.org/10.1016/j.ijsolstr.2009.12.011>.
- Dunand, M., Mohr, D., 2011. Optimized butterfly specimen for the fracture testing of sheet materials under combined normal and shear loading. *Engineering Fracture Mechanics* 78, 2919–2934. doi:<https://doi.org/10.1016/j.engfracmech.2011.08.008>.
- Eggersmann, R., Kirchdoerfer, T., Reese, S., Stainier, L., Ortiz, M., 2019. Model-free data-driven inelasticity. *Computer Methods in Applied Mechanics and Engineering* 350, 81–99. doi:[10.1016/j.cma.2019.02.016](https://doi.org/10.1016/j.cma.2019.02.016).
- Eggersmann, R., Stainier, L., Ortiz, M., Reese, S., 2021. Model-free data-driven computational mechanics enhanced by tensor voting. *Computer Methods in Applied Mechanics and Engineering* 373, 113499. doi:[10.1016/j.cma.2020.113499](https://doi.org/10.1016/j.cma.2020.113499).
- Flaschel, M., Kumar, S., De Lorenzis, L., 2021. Unsupervised discovery of interpretable hyperelastic constitutive laws. *Computer Methods in Applied Mechanics and Engineering* 381, 113852. doi:<https://doi.org/10.1016/j.cma.2021.113852>.
- Flaschel, M., Kumar, S., De Lorenzis, L., 2023. Automated discovery of generalized standard material models with euclid. *Computer Methods in Applied Mechanics and Engineering* 405, 115867. doi:<https://doi.org/10.1016/j.cma.2022.115867>.
- Fu, J., Barlat, F., Kim, J.H., Pierron, F., 2016. Identification of nonlinear kinematic hardening constitutive model parameters using the virtual fields method for advanced high strength steels. *International Journal of Solids and Structures* 102, 30–43. doi:<https://doi.org/10.1016/j.ijsolstr.2016.10.020>.
- Fu, J., Xie, W., Zhou, J., Qi, L., 2020. A method for the simultaneous identification of anisotropic yield and hardening constitutive parameters for sheet metal forming.

- International Journal of Mechanical Sciences 181, 105756. doi:<https://doi.org/10.1016/j.ijmecsci.2020.105756>.
- Fuhg, J.N., Anantha Padmanabha, G., Bouklas, N., Bahmani, B., Sun, W., Vlassis, N.N., Flaschel, M., Carrara, P., De Lorenzis, L., 2024. A review on data-driven constitutive laws for solids. *Archives of Computational Methods in Engineering* , 1–43doi:<https://doi.org/10.1007/s11831-024-10196-2>.
- Galilei, G., 1638. *Discorsi e dimostrazioni matematiche intorno a due nuove scienze attinenti la meccanica e i movimenti locali*. Leiden: appresso gli Elsevirii.
- Gorji, M.B., Mohr, D., 2017. Micro-tension and micro-shear experiments to characterize stress-state dependent ductile fracture. *Acta Materialia* 131, 65–76. doi:10.1016/j.actamat.2017.03.034.
- Guery, A., Hild, F., Latourte, F., Roux, S., 2016. Identification of crystal plasticity parameters using dic measurements and weighted femu. *Mechanics of Materials* 100, 55–71. doi:<https://doi.org/10.1016/j.mechmat.2016.06.007>.
- Gurtin, M.E., Fried, E., Anand, L., 2010. *The mechanics and thermodynamics of continua*. Cambridge University Press.
- Haux, R., 2010. Medical informatics: past, present, future. *International journal of medical informatics* 79, 599–610. doi:<https://doi.org/10.1016/j.ijmedinf.2010.06.003>.
- Hencky, H., 1924. Zur theorie plastischer deformationen und der hierdurch im material hervorgerufenen nachspannungen. *ZAMM-Journal of Applied Mathematics and Mechanics/Zeitschrift für Angewandte Mathematik und Mechanik* 4, 323–334. doi:<https://doi.org/10.1002/zamm.19240040405>.
- Hill, R., 1948. A theory of the yielding and plastic flow of anisotropic metals. *Proceedings of the Royal Society of London. Series A. Mathematical and Physical Sciences* 193, 281–297. doi:<https://doi.org/10.1098/rspa.1948.0045>.
- Huang, D.Z., Xu, K., Farhat, C., Darve, E., 2020. Learning constitutive relations from indirect observations using deep neural networks. *Journal of Computational Physics* 416, 109491. doi:10.1016/j.jcp.2020.109491.

- Huber, M.T., 1904. Właściwa praca odkształcenia jako miara wyteżenia materiału. translated as “specific work of strain as a measure of material effort”. *Archives of Mechanics* 56, 173–190.
- Ihuaenyi, R., Deng, J., Bae, C., Xiao, X., 2023a. An orthotropic nonlinear thermo-viscoelastic model for polymeric battery separators. *Journal of the Electrochemical Society* 170, 010520. doi:<https://doi.org/10.1149/1945-7111/acb178>.
- Ihuaenyi, R., Yan, S., Deng, J., Bae, C., Sakib, I., Xiao, X., 2021. Orthotropic thermo-viscoelastic model for polymeric battery separators with electrolyte effect. *Journal of The Electrochemical Society* 168, 090536. doi:<https://doi.org/10.1149/1945-7111/ac24b6>.
- Ihuaenyi, R.C., Deng, J., Bae, C., Xiao, X., 2023b. A coupled nonlinear viscoelastic–viscoplastic thermomechanical model for polymeric lithium-ion battery separators. *Batteries* 9, 475. doi:<https://doi.org/10.3390/batteries9090475>.
- Ihuaenyi, R.C., Luo, J., Li, W., Zhu, J., 2024. Seeking the most informative design of test specimens for learning constitutive models. *Extreme Mechanics Letters* 69, 102169. doi:<https://doi.org/10.1016/j.eml.2024.102169>.
- Iqbal, S., Li, B., Sonta, K., Ihuaenyi, R., Xiao, X., 2023. Probabilistic finite element analysis of sheet molding compound composites with an extended strength distribution model. *Finite Elements in Analysis and Design* 214, p.103865. doi:<https://doi.org/10.1016/j.finel.2022.103865>.
- Jones, E., Carroll, J.D., Karlson, K.N., Kramer, S.L.B., Lehoucq, R.B., Reu, P.L., Turner, D.Z., 2018. Parameter covariance and non-uniqueness in material model calibration using the virtual fields method. *Computational Materials Science* 152, 268–290. doi:<https://doi.org/10.1016/j.commatsci.2018.05.037>.
- Kamaya, M., Kawakubo, M., 2011. A procedure for determining the true stress–strain curve over a large range of strains using digital image correlation and finite element analysis. *Mechanics of Materials* 43, 243–253. doi:[10.1016/j.mechmat.2011.02.007](https://doi.org/10.1016/j.mechmat.2011.02.007).
- Kim, J.H., Barlat, F., Pierron, F., Lee, M.G., 2014. Determination of anisotropic plastic

- constitutive parameters using the virtual fields method. *Experimental Mechanics* 54, 1189–1204. doi:<https://doi.org/10.1007/s11340-014-9879-x>.
- Kirchdoerfer, T., Ortiz, M., 2016. Data-driven computational mechanics. *Computer Methods in Applied Mechanics and Engineering* 304, 81–101. doi:10.1016/j.cma.2016.02.001.
- Kirchdoerfer, T., Ortiz, M., 2017. Data driven computing with noisy material data sets. *Computer Methods in Applied Mechanics and Engineering* 326, 622–641. doi:10.1016/j.cma.2017.07.039.
- Kirchdoerfer, T., Ortiz, M., 2018. Data-driven computing in dynamics. *International Journal for Numerical Methods in Engineering* 113, 1697–1710. doi:10.1002/nme.5716.
- Kramer, S.L., Scherzinger, W.M., 2014. Implementation and evaluation of the virtual fields method: determining constitutive model parameters from full-field deformation data. Technical Report SAND2014-17871. Sandia National Laboratories. doi:<https://doi.org/10.2172/1158669>.
- Kuwabara, T., 2007. Advances in experiments on metal sheets and tubes in support of constitutive modeling and forming simulations. *International Journal of Plasticity* 23, 385–419. doi:10.1016/j.ijplas.2006.06.003.
- Kuwabara, T., Ikeda, S., Kuroda, K., 1998. Measurement and analysis of differential work hardening in cold-rolled steel sheet under biaxial tension. *Journal of Materials Processing Technology* 80-81, 517–523. doi:10.1016/S0924-0136(98)00155-1.
- Lagarias, J., Reeds, J., Wright, M., Wright, P., 1998. Convergence properties of the nelder–mead simplex method in low dimensions. *SIAM Journal on Optimization* 9, 112–147. doi:<https://doi.org/10.1137/S1052623496303470>.
- Lattanzi, A., Barlat, F., Pierron, F., Marek, A., Rossi, M., 2020. Inverse identification strategies for the characterization of transformation-based anisotropic plasticity models with the non-linear vfm. *International Journal of Mechanical Sciences* 173, 105422. doi:10.1016/j.ijmecsci.2020.105422.
- Lava, P., Jones, E., Wittevrongel, L., Pierron, F., 2020. Validation of finite-element models using full-field experimental data: Levelling finite-element analysis data through a



- digital image correlation engine. *Strain* 56, e12350. doi:<https://doi.org/10.1111/str.12350>.
- Li, W., Zhu, J., Xia, Y., Gorji, M.B., Wierzbicki, T., 2019. Data-driven safety envelope of lithium-ion batteries for electric vehicles. *Joule* 3, 2703–2715. doi:10.1016/j.joule.2019.07.026.
- Marino, E., Flaschel, M., Kumar, S., De Lorenzis, L., 2023. Automated identification of linear viscoelastic constitutive laws with euclid. *Mechanics of Materials* 181, 104643. doi:<https://doi.org/10.1016/j.mechmat.2023.104643>.
- Martins, J., Andrade-Campos, A., Thuillier, S., 2019. Calibration of anisotropic plasticity models using a biaxial test and the virtual fields method. *International Journal of Solids and Structures* 172, 21–37. doi:<https://doi.org/10.1016/j.ijsolstr.2019.05.019>.
- Hernandez-de Menendez, M., Escobar Díaz, C.A., Morales-Menendez, R., 2020. Engineering education for smart 4.0 technology: a review. *International Journal on Interactive Design and Manufacturing* 14, 789–803. doi:<https://doi.org/10.1007/s12008-020-00672-x>.
- Meng, Y., Xia, Y., Zhou, Q., Lin, S., 2016. Identification of true stress-strain curve of thermoplastic polymers under biaxial tension. *SAE International Journal of Materials and Manufacturing* 9, 768–775. doi:10.4271/2016-01-0514.
- von Mises, R.E., 1913. *Mechanik der festen körper im plastisch-deformablen zustand*. Nachrichten von der Gesellschaft der Wissenschaften zu Göttingen, Mathematisch-Physikalische Klasse 1913, 582–592.
- Morin, L., Leblond, J.B., Mohr, D., Kondo, D., 2017. Prediction of shear-dominated ductile fracture in a butterfly specimen using a model of plastic porous solids including void shape effects. *European Journal of Mechanics-A/Solids* 61, 433–442. doi:<https://doi.org/10.1016/j.euromechsol.2016.10.014>.
- Mulder, J., Vegter, H., Aretz, H., Keller, S., Van Den Boogaard, A., 2015. Accurate determination of flow curves using the bulge test with optical measuring systems. *Journal*

- of Materials Processing Technology 226, 169–187. doi:<https://doi.org/10.1016/j.jmatprotec.2015.06.034>.
- Ni, X., Kopp, R., Kalfon-Cohen, E., Furtado, C., Lee, J., Arteiro, A., Borstnar, G., Mavrogordato, M.N., Helfen, L., Sinclair, I., Spearing, S.M., Camanho, P.P., Wardle, B.L., 2021. In situ synchrotron computed tomography study of nanoscale interlaminar reinforcement and thin-ply effects on damage progression in composite laminates. *Composites Part B: Engineering* 217, 108623. doi:[10.1016/j.compositesb.2021.108623](https://doi.org/10.1016/j.compositesb.2021.108623).
- Pan, B., Qian, K., Xie, H., Asundi, A., 2009. Two-dimensional digital image correlation for in-plane displacement and strain measurement: a review. *Measurement Science and Technology* 20, 062001. doi:[10.1088/0957-0233/20/6/062001](https://doi.org/10.1088/0957-0233/20/6/062001).
- Papasidero, J., Doquet, V., Mohr, D., 2015. Ductile fracture of aluminum 2024-t351 under proportional and non-proportional multi-axial loading: Bao-wierzbicki results revisited. *International Journal of Solids and Structures* 69, 459–474. doi:<https://doi.org/10.1016/j.ijsolstr.2015.05.006>.
- Peirs, J., Verleysen, P., Degrieck, J., 2012. Novel technique for static and dynamic shear testing of ti6al4v sheet. *Experimental Mechanics* 52, 729–741. doi:<https://doi.org/10.1007/s11340-011-9541-9>.
- Plancher, E., Qu, K., Vonk, N.H., Gorji, M.B., Tancogne-Dejean, T., Tasan, C.C., 2020. Tracking microstructure evolution in complex biaxial strain paths: A bulge test methodology for the scanning electron microscope. *Experimental Mechanics* 60, 35–50. doi:<https://doi.org/10.1007/s11340-019-00538-8>.
- Pottier, T., Toussaint, F., Vacher, P., 2011. Contribution of heterogeneous strain field measurements and boundary conditions modelling in inverse identification of material parameters. *European Journal of Mechanics-A/Solids* 30, 373–382. doi:<https://doi.org/10.1016/j.euromechsol.2010.10.001>.
- Qi, Y., Hector, L.G., James, C., Kim, K.J., 2014. Lithium concentration dependent elastic properties of battery electrode materials from first principles calculations. *Journal of the Electrochemical Society* 161, F3010. doi:<http://dx.doi.org/10.1149/2.0031411jes>.

- Ramprasad, R., Batra, R., Pilania, G., Mannodi-Kanakkithodi, A., Kim, C., 2017. Machine learning in materials informatics: recent applications and prospects. *npj Computational Materials* 3, 54. doi:<https://doi.org/10.1038/s41524-017-0056-5>.
- Robert, C.P., 1999. *Monte Carlo Statistical Methods*. Springer.
- Rossi, M., Lattanzi, A., Morichelli, L., Martins, J.M., Thuillier, S., Andrade-Campos, A., Coppieters, S., 2022. Testing methodologies for the calibration of advanced plasticity models for sheet metals: A review. *Strain* 58, e12426. doi:<https://doi.org/10.1111/str.12426>.
- Rossi, M., Lava, P., Pierron, F., Debruyne, D., Sasso, M., 2015. Effect of dic spatial resolution, noise and interpolation error on identification results with the vfm. *Strain* 51, 206–222. doi:<https://doi.org/10.1111/str.12134>.
- Rossi, M., Pierron, F., 2012. On the use of simulated experiments in designing tests for material characterization from full-field measurements. *International Journal of Solids and Structures* 49, 420–435. doi:<https://doi.org/10.1016/j.ijsolstr.2011.09.025>.
- Roth, C., Mohr, D., 2018. Determining the strain to fracture for simple shear for a wide range of sheet metals. *International Journal of Mechanical Sciences* 149, 224–240. doi:<https://doi.org/10.1016/j.ijmecsci.2018.10.007>.
- Roth, C.C., Mohr, D., 2016. Ductile fracture experiments with locally proportional loading histories. *International Journal of Plasticity* 79, 328–354. doi:<https://doi.org/10.1016/j.ijplas.2015.08.004>.
- Segal, V., 2002. Severe plastic deformation: simple shear versus pure shear. *Materials Science and Engineering: A* 338, 331–344. doi:10.1016/S0921-5093(02)00066-7.
- Simo, J.C., Hughes, T.J., 2006. *Computational inelasticity*. volume 7. Springer Science & Business Media.
- Singer, S., Nelder, J., 2009. Nelder–mead algorithm. *Scholarpedia* 4, 2928.

- Stainier, L., Leygue, A., Ortiz, M., 2019. Model-free data-driven methods in mechanics: material data identification and solvers. *Computational Mechanics* 64, 381–393. doi:<https://doi.org/10.1007/s00466-019-01731-1>.
- Sutton, M.A., Orteu, J.J., Schreier, H., 2009. Image correlation for shape, motion and deformation measurements: basic concepts, theory and applications. Springer Science & Business Media.
- Tancogne-Dejean, T., Roth, C.C., Morgeneyer, T.F., Helfen, L., Mohr, D., 2021. Ductile damage of aa2024-t3 under shear loading: Mechanism analysis through in-situ laminography. *Acta Materialia* 205, 116556. doi:<https://doi.org/10.1016/j.actamat.2020.116556>.
- Torrey, L., Shavlik, J., 2010. Transfer learning, in: *Handbook of Research on Machine Learning Applications and Trends: Algorithms, Methods, and Techniques*. IGI Global, pp. 242–264. doi:[10.4018/978-1-60566-766-9.ch011](https://doi.org/10.4018/978-1-60566-766-9.ch011).
- Vilotic, D., Planck, M., Grbic, S., Alexandrov, S., Chikanova, N., 2003. An approach to determining the workability diagram based on upsetting tests. *Fatigue & Fracture of Engineering Materials & Structures* 26, 305–310. doi:[10.1046/j.1460-2695.2003.00469.x](https://doi.org/10.1046/j.1460-2695.2003.00469.x).
- Wierzbicki, T., Bao, Y., Lee, Y.W., Bai, Y., 2005. Calibration and evaluation of seven fracture models. *International Journal of Mechanical Sciences* 47, 719–743. doi:[10.1016/j.ijmecsci.2005.03.003](https://doi.org/10.1016/j.ijmecsci.2005.03.003). a Special Issue in Honour of Professor Stephen R. Reid’s 60th Birthday.
- Xu, K., Huang, D.Z., Darve, E., 2021. Learning constitutive relations using symmetric positive definite neural networks. *Journal of Computational Physics* 428, 110072. doi:[10.1016/j.jcp.2020.110072](https://doi.org/10.1016/j.jcp.2020.110072).
- Yamanaka, A., Kamijyo, R., Koenuma, K., Watanabe, I., Kuwabara, T., 2020. Deep neural network approach to estimate biaxial stress-strain curves of sheet metals. *Materials & Design* 195, 108970. doi:[10.1016/j.matdes.2020.108970](https://doi.org/10.1016/j.matdes.2020.108970).
- Zhang, L., Min, J., Carsley, J., Stoughton, T., Lin, J., 2017. Experimental and theoretical investigation on the role of friction in nakazima testing. *International Journal*

- of Mechanical Sciences 133, 217–226. doi:<https://doi.org/10.1016/j.ijmecsci.2017.08.020>.
- Zhang, Z., Hauge, M., Ødegård, J., Thaulow, C., 1999. Determining material true stress–strain curve from tensile specimens with rectangular cross-section. *International Journal of Solids and Structures* 36, 3497–3516. doi:[10.1016/S0020-7683\(98\)00153-X](https://doi.org/10.1016/S0020-7683(98)00153-X).
- Zhao, H., Braatz, R.D., Bazant, M.Z., 2021. Image inversion and uncertainty quantification for constitutive laws of pattern formation. *Journal of Computational Physics* 436, 110279. doi:[10.1016/j.jcp.2021.110279](https://doi.org/10.1016/j.jcp.2021.110279).
- Zhao, H., Deng, H.D., Cohen, A.E., Lim, J., Li, Y., Fraggadakis, D., Jiang, B., Storey, B.D., Chueh, W.C., Braatz, R.D., et al., 2023. Learning heterogeneous reaction kinetics from x-ray videos pixel by pixel. *Nature* 621, 289–294. doi:<https://doi.org/10.1038/s41586-023-06393-x>.
- Zhao, H., Storey, B.D., Braatz, R.D., Bazant, M.Z., 2020. Learning the physics of pattern formation from images. *Phys. Rev. Lett.* 124, 060201. doi:[10.1103/PhysRevLett.124.060201](https://doi.org/10.1103/PhysRevLett.124.060201).
- Zhu, J., Xia, Y., Luo, H., Gu, G., Zhou, Q., 2014. Influence of flow rule and calibration approach on plasticity characterization of dp780 steel sheets using hill48 model. *International Journal of Mechanical Sciences* 89, 148–157. doi:<https://doi.org/10.1016/j.ijmecsci.2014.09.001>.
- Zhu, J., Zhang, X., Luo, H., Sahraei, E., 2018. Investigation of the deformation mechanisms of lithium-ion battery components using in-situ micro tests. *Applied Energy* 224, 251–266. doi:[10.1016/j.apenergy.2018.05.007](https://doi.org/10.1016/j.apenergy.2018.05.007).